Climate Dynamics (2004) 23: 569–599
DOI 10.1007/s00382-004-0455-4

L. D. D. Harvey

Characterizing the annual-mean climatic effect of anthropogenic CO_2 and aerosol emissions in eight coupled atmosphere-ocean GCMs

Received: 27 January 2003 / Accepted: 21 April 2004 / Published online: 4 August 2004
© Springer-Verlag 2004

Abstract This work examines the spatial patterns of the transient response of mean annual temperature and precipitation to CO_2 (or CO_2 plus aerosol or aerosol proxy) radiative forcing in eight coupled AOGCMs, generally for the period 1900–2099. Response patterns are characterized using empirical orthogonal functions (EOFs) and the quasi-EOFs of Harvey and Wigley (the first qEOF field, discussed here, is given by the correlation between local year-by-year temperature changes and the global mean temperature change). The first temperature EOF accounts for 80–95% of the space-time variation of the CO_2 run in all of the models, and is almost identical to $qEOF_1$ of the temperature response or to the temperature change pattern averaged over the last 30 years of the simulations. EOF_1 accounts for 80–95% of the space-time variation in the CO_2 + aerosol runs in six of the eight models. The CO_2 response patterns of different models are highly correlated with one another (R^2 generally >0.5), and are also highly correlated with the CO_2 + aerosol response patterns ($R^2 \geq 0.85$ in all except one model). The difference between CO_2 and CO_2 + aerosol runs can be represented by EOF_1 of the year-by-year differences, by $qEOF_1$ of the year-by-year differences, or by the difference in temperature averaged over the last 30 years of each run. In models where these representations are highly correlated with each other, they are also highly correlated with CO_2 EOF_1. In other cases, aerosol EOF_1 is modestly to highly correlated with control EOF_1 (i.e.: the year-by-year differences between CO_2 and CO_2 + aerosol runs are dominated by internal variability), while aerosol $qEOF_1$ and the 30-year difference are highly correlated with each other. For all models, the decadal mean temperature change can be closely replicated by scaling the CO_2 EOF_1 pattern based on the global mean temperature changes (RMSE for the last decade is $<6\%$ of the RMS temperature change for CO_2 runs, $<8\%$ for CO_2 + aerosol runs). The first EOF of the precipitation response to increasing CO_2 accounts for only 10–30% of the space-time variation, and is generally highly correlated (R^2 up to 0.85) with control EOF_1. In all of the models, there is an increase in precipitation in the ITCZ and a decrease in bands at or near 30°S and 30°N. In many models there is an El Niño-like response, including a substantial decrease in precipitation over the Amazon. Global-mean precipitation increases in all models due to CO_2 forcing, but aerosols appear to have a disproportionally large effect in suppressing the increase compared to their effect in suppressing the warming. There is evidence in some models that the non-absorbing aerosols considered here reduce summer monsoon rainfall compared to the changes that would be expected based on the globally averaged effect of aerosols on precipitation. When regional precipitation changes over time are predicted by scaling a fixed precipitation-change pattern with the global mean temperature change, the global mean RMSE in the predicted change in decadal-mean precipitation is 25–35% of the global RMS precipitation changes by the end of the simulation.

L. D. D. Harvey
Department of Geography University of Toronto,
100 St. George Street, Toronto M5S 3G3,
Canada
E-mail: harvey@geog.utoronto.ca

1 Introduction

It is now generally accepted that the net anthropogenic effect on climate includes the effect of several different kinds of aerosols, whose concentrations in the atmosphere have been affected by human activities, as well as the effect of greenhouse gas (GHG) increases. Human-induced changes in the land vegetation cover have also likely led to changes in temperature that rival the current effect of greenhouse gas increases in some regions during some seasons (Chase et al. 2000; Pitman and Zhao 2000). In this work, the spatial patterns of temperature

and precipitation change resulting from the first two of these anthropogenic perturbations, increases in the atmospheric concentration of CO_2 (as a proxy for all GHGs) and aerosols, are analyzed.

The radiative effect of an increase in CO_2 differs by less than a factor of two, while the radiative effect of aerosols exhibits much stronger regional variation, due primarily to the strong regional variation in the anthropogenic aerosol loading. The aerosol most significantly altered by human activities is likely to be the sulfate aerosol, which has a cooling effect on climate. Recent analyses of observed temperature changes during the past 140 years suggest that the global-mean net cooling effect of all anthropogenic aerosols grew to about 1.5 $W\,m^{-2}$ by 1990, compared to a heating effect from GHGs of about 2.6 $W\,m^{-2}$ in 1990 (Andronova and Schlesinger 2000; Harvey and Kaufmann 2002). However, the local annual aerosol cooling effect can be up to twice the local GHG heating effect, giving a sizeable net cooling effect. Temperatures need not have cooled in these regions, however, due to the advection of heat from elsewhere, but the warming could be strongly suppressed. Thus, a much more complex pattern of temperature changes might result from the combined effect of GHGs and aerosols, than from GHGs alone. An important research problem is to quantify the spatial pattern of temperature effects resulting from anthropogenic aerosols, and to compare this with the temperature change patterns associated with GHG increases alone.

Recently, the results of transient simulations of climatic change by several AOGCMs have been made available through the Intergovernmental Panel on Climate Change (IPCC) Data Distribution Centre (DDC) website (http://ipcc-ddc.cru.uea.ac.uk/). With one exception, these simulations generally begin in 1860–1900, and extend in most cases to 2100. Results are available from most models for a control run and for one or more runs with CO_2 forcing only and with CO_2 plus direct sulfur aerosol forcing. In this study, changes in temperature and precipitation for the CO_2 -only runs for seven models from the IPCC DDC website are examined. The difference in the temperature and precipitation response between the CO_2 + aerosol and the CO_2 -only runs is determined, and compared with the CO_2 -only difference fields and with the aerosol radiative forcing fields. An eighth model (the NCAR PCM) provides results only for CO_2 + aerosol forcing. In order to compare the different models succinctly and objectively, empirical orthogonal functions (EOFs) of the time-space variation in temperature and precipitation for the CO_2 (or CO_2 + aerosol) runs, and of the time-space variation of the difference in temperature and precipitation between the CO_2 and CO_2 + aerosol runs (when available), are computed. The eight models, key characteristics of the models, and supporting references are listed in Table 1.

Harvey and Wigley (2003) and Harvey (2003) analyzed the control-run temperature and precipitation

Table 1 Characteristics of the models and simulations used here. Shown are the CO_2 concentration or forcing scenarios used after 1990. "IS92a" means that the CO_2 changes used were those that give the same forcing as the total of all GHGs in the IS92a scenario

Model	Latitude-longitude grid	Number of runs			Ending date (at end of indicated year)		Post-1990 CO_2 radiative forcing	Flux adjustment?	Key references
		C	G	GA	G	GA			
CCC	48 × 96	1	1	3	2099	2099	+1%/yr	Yes	Reader and Boer (1998), Boer et al. (2000a, b)
CCSR	32×64	1	1	1	2099	2099	+1%/yr	Yes	Emori et al. (1999)
CSIRO	56×64	1	1	1	2099	2099	+1%/yr	Yes	Hirst et al. (1996)
ECHAM3	32×64	1	1	1	2079	2049	IS92a	Yes	Timmermann et al. (1999)
ECHAM4	64×128	1	1	1	2099	2049	IS92a	Yes	Roeckner et al. (1999)
HadCM2	73×96	1	4	4	2099	2099	IS92a	Yes	Johns et al. (1997)
HadCM3	73×96[a]	1	1	1	2099	2099	IS92a	no	Cox et al. (1999), Hulme et al. (1999), Gordon et al. (2000)
PCM	64×128	1	0	1	n/a	2099	+1%/yr	no	Washington et al. (2000), Meehl et al. (2002)

CCC = Canadian Climate Centre (Victoria, BC) model
CCSR = Centre for Climate Research Studies (University of Tokyo) model
CSIRO = Commonwealth Scientific and Industrial Research Organization (Australia) model
ECHAM3 is the ECHAM3/LSG model, where ECHAM = *E*uropean *C*entre for Medium RangeWeather Forecasts, University of *Ham*burg atmospheric model and LSG is a *L*arge *S*cale *G*eostrophic ocean model
ECHAM4 is the ECHAM4/OPYC3 model, where OPYC3 is an isopycnal-coordinate ocean model
HadCM2 = Hadley Centre, Model 2 (Bracknell, UK)
HadCM3 = Hadley Centre, Model 3 (Bracknell, UK)
PCM = Parallel Climate Model, National Center for Atmospheric Research (Boulder, Colorado)
C = control
G = CO_2 run
GA = CO_2 + aerosol run
[a] The oceanic component has a grid resolution of 1.25° latitude ×1.25° longitude (144 × 288), and is formulated in isopycnal coordinates

variability, respectively, of the same eight AOGCMs. They found that the principal temperature EOFs often bear little resemblance to the principal EOFs in the observed data. This is due in part to the presence of artificially large variability in ice-margin areas and/or in continental interiors in some models, and to modes of variability that appear in separate EOFs in the observations being combined in part within the same EOF in the models. Given that variability corresponding to observed modes of variability (e.g. the El Niño and North Atlantic oscillations) could be present in the models but not show up in the principal EOFs due to their smaller amplitude, Harvey and Wigley (2003) devised on alternative to EOF analysis that looks for predetermined modes of variability in the time-space data. These patterns were called "quasi-empirical orthogonal functions" or qEOFs. The qEOF analysis is applied here, along with EOF analysis, to characterize the impact of CO_2 and aerosol forcing on temperature patterns, both separately and together. An overview of these methods is provided next.

2 Methods used

Monthly average grid point data for all the years of the control, CO_2, and CO_2 + aerosol runs were downloaded from the IPCC DDC website, and annual means were computed. The linear trend in the control run simulation was computed at each grid point and subtracted from the CO_2 and CO_2 + aerosol simulations (except in the case of the PCM, where the control simulation did not serve as the initial condition for the CO_2 + aerosol forcing simulation). The data were then subjected to EOF analysis using a programme kindly provided by Aiguo Dai, the same programme as used in Harvey and Wigley (2003). For models and forcings where there is more than one member of an ensemble, the detrended data from all the members of the ensemble are strung together to form a single dataset, which was then subjected to EOF analysis. In all cases, unnormalized data (i.e. not divided by the local standard deviation) are used in the analysis. The EOFs so-produced are divided by the maximum absolute value of the EOF field and the amplitude (principle component) time series multiplied by the same factor. The EOF amplitudes presented here thus have physical dimensions, and represent the maximum change associated with the corresponding EOF found anywhere at a given time.

The quasi-EOF analysis generates a series of spatial patterns based on the covariance between local temperature and the temperature averaged over various reference regions. For the first quasi-EOF ($qEOF_1$), the reference region is the entire world. Thus, the first pattern is the spatial field of the time series covariance between the temperature at each grid point and the global-mean temperature. The product between this spatial pattern and the annual- and global-mean temperature deviation from the time series mean (which is the $qEOF_1$ amplitude), gives the temperature variation for that year ($q\mathrm{T}(x, y, t_i)$) associated with $qEOF_1$. This temperature variation is then subtracted from the original annual temperature variation, $qEOF_2$ is computed based on the covariance between the residual grid-point temperature variation ($\Delta T_2(x,y,t_i)$) and the residual variation computed over some new region, the associated yearly temperature change is subtracted from the previous residual, and the process repeated. The averaging region used $qEOF_2$ is the tropical eastern Pacific (5°S–5°N by 90–150°W, corresponding to the Niño 3 region), so $qEOF_2$ represents El Niño-related variability. Higher qEOFs are not used here. Full details are found in Harvey and Wigley (2003).

It is desirable that $qEOF_1$ represent the spatial pattern of climatic change at decadal and longer time scales, without the effects of interannual variability partly transferred to $qEOF_1$. Since El Niño likely causes short-term fluctuations in global-mean temperature (due to its association with changes in the mixed layer-deep ocean heat flux), part of the variability associated with it could be transferred to $qEOF_1$. To avoid or least greatly minimize this, smoothed temperature deviations (computed using a 9-year running mean) have been used to compute $qEOF_1$ and $qT(x,y,t_i)$. Thus, $\Delta T_2(x,y,t_i)$ is given by the original temperature deviations minus a $qT(x,y,t_i)$ that is given by the $qEOF_1$ computed from smoothed data times the smoothed variation in global-mean temperature. This residual is used to compute $qEOF_1$. Subtracting $qT(x,y,t_i)$ from the original data will not noticeably alter the amplitude of year-to-year variations, so that $qEOF_2$ will pick up the spatial patterns associated with El Niño-related interannual variability. Of course, if there is a persistent response pattern that resembles El Niño variability, and if it is correlated with the increase in global-mean temperature, this part of the response will be transferred to $qEOF_1$. Thus, if the temperature response becomes more El Niño-like on average, this will show up as an El Niño-like component in the spatial field for $qEOF_1$, rather than as an increase in the amplitude of the second (El Niño) qEOF. On the other hand, the development of decadal oscillations in any of the natural modes of variability (for example) or a change in the amplitude of interannual variability, will show up as changes in the amplitudes for qEOFs beyond $qEOF_1$.

In addition to presenting EOF and qEOF results, we also present time series of globally averaged temperature and precipitation changes, and latitudinal profiles of the precipitation changes averaged over various time periods. For all the models except the PCM, we computed temperature and precipitation changes for the CO_2 and CO_2 + aerosol runs relative to the average over the 1890–1919 period. For the PCM, the reference period is 1960–1989, as the forcing begins in 1990 rather than around 1900. The changes by the end of the simulation (at 2100) are smaller than they would be otherwise.

3 Overview of model temperature and precipitation response

The model GHG results studied were generated using CO_2 forcing alone. Up to 1990, CO_2 changes followed the observed effective CO_2 increase (i.e. the CO_2 increase that gives the same radiative forcing as the sum of all GHGs). This was followed by an increase in atmospheric CO_2 concentration by 1% per year, compounded, or by the effective CO_2 changes associated with the IS92a emissions scenario (Leggett et al. 1992), as indicated in Table 1. If the CO_2 concentration in 1800 was 280 ppmv, if the forcing by GHGs relative to 1800 was $2.5W\ m^{-2}$ if 1990, and if the forcing for a CO_2 doubling is $3.5W\ m^{-2}$, then the effective CO_2 concentration in 1990 was 460 ppmv. At 1%/year compounded increase, it reaches 1382 ppmv by 2100, an increase by a factor of 3.0. This gives a radiative forcing of $5.54W\ m^{-2}$ relative to 1990. For the IS92a scenario, the GHG radiative forcing in 2100 relative to 1990 is about $6.5W\ m^{-2}$, depending on the exact assumptions used in relating emissions to concentration, and concentration to forcing (see Harvey 2000, Ch 7).

Table 2 outlines how the aerosol radiative forcing has been imposed or computed in the various models, as well as the global-mean aerosol radiative forcing in 1990 and during the mid twenty first century (where known). All models used the IS92a scenario for aerosol precursor emissions. In most cases, aerosol distributions and associated direct radiative forcings are computed for two or more time periods in an offline mode, then linearly interpolated between these time periods. In most models, aerosol forcing is simulated by surface albedo changes sufficient to produce the same top-of-atmosphere radiative forcing. In two cases (CCSR and HadCM3), aerosols are inserted into the atmosphere and explicit radiative transfer calculations are performed instead of altering the surface albedo, and in another case (ECHAM4), the aerosol distribution is computed interactively with the climate simulation and explicit radiative transfer calculations are performed.

Only direct aerosol forcing is used (or simulated) for the runs analyzed here except for HadCM3 (see Table 2), so the forcing will vary linearly with the assumed aerosol loading and almost linearly with the assumed emission (see Harvey 2000, Sect. 7.7 and 8.11). The forcing after 1990 in different models will differ in proportion to the difference in forcings assumed for 1990, which are given in Table 2. In HadCM2, the forcing grows from $-0.64W\ m^{-2}$ in 1990 to $-1.49W\ m^{-2}$ by 2050, then decreases slightly to $-1.45W\ m^{-2}$ by 2100 (Mitchell and Johns 1997). This mirrors the assumed increase in sulfur emission from 75 Tg S year $^{-1}$ in 1990 to 153 Tg S $year^{-1}$ in 2050 and decrease to 147 Tg S $year^{-1}$ in 2100. More recent work (e.g. Nakićenović et al. 2000; Houghton et al. 2001) foresees much smaller increases in sulfur emissions or a decrease, so the IS92 emission scenario, used in all the models studied here, is high by current standards.

The aerosol forcing patterns in CCSR and HadCM2 are compared in Fig. 1, and the zonal-mean radiative forcing in these two models along with the relative aerosol loading in CCC are compared in Fig. 2. As seen from Figs. 1 and 2, the radiative forcing is highly concentrated in the NH, with peak zonal-mean forcing of about $-4W\ m^{-2}$ by the mid twenty first century for HadCM2 and about $-2W\ m^{-2}$ for CCSR.

Figure 3 compares the global-mean temperature response over the period 1900–2100 (or some subset thereof), as simulated by the eight AOGCMs. Results are shown for the CO_2 runs (Fig. 3a), the CO_2 + aerosol runs (Fig. 3b), and the difference between these runs (Fig. 3c). Also shown in Fig. 3 is the observed global-mean temperature variation from 1900 to 2002. As noted, some of the models had a noticeable downward trend in the control run, which was subtracted grid-point by grid-point from the CO_2 and CO_2 + aerosol results before computing the global-mean trends shown in Fig. 3 (and before doing the EOF and qEOF analysis to be described later).

As can be seen from Fig. 3, the models as a whole simulate slightly too large a global- mean warming between 1900–2000 when driven by CO_2 increases alone,

Table 2 Treatment of aerosols, and global average aerosol radiative forcing relative to the start of the simulation, in the eight models

Model	Treatment of aerosols	Global-mean aerosol radiative forcing ($W\ m^{-2}$)	
		1990	Mid-century
CCC	Alteration of α_s to mimic direct forcing	–0.6	–1.5, 2050
CCSR	Explicit scattering, direct effect only, non-interactive aerosol distribution	–0.46	–0.91, 2060
CSIRO	Alteration of α_s to mimic direct forcing	–0.40	?
ECHAM3	Alteration of α_s to mimic direct forcing	–0.7	?
ECHAM4	Explicit scattering, direct effect only, interactive aerosol distribution	–0.35[a]	–0.95, 2050
HadCM2	Alteration of $_s$ to mimic direct forcing	–0.64	–1.49, 2050
HadCM3	Explicit scattering, direct effect + indirect effect	–1.10	–1.29, 2050
PCM	Alteration of α_s, twice as large as needed to mimic direct forcing, so as to account for indirect forcing	n/a	–0.52 in 2030, relative to 1990

[a] Pertains to 1980

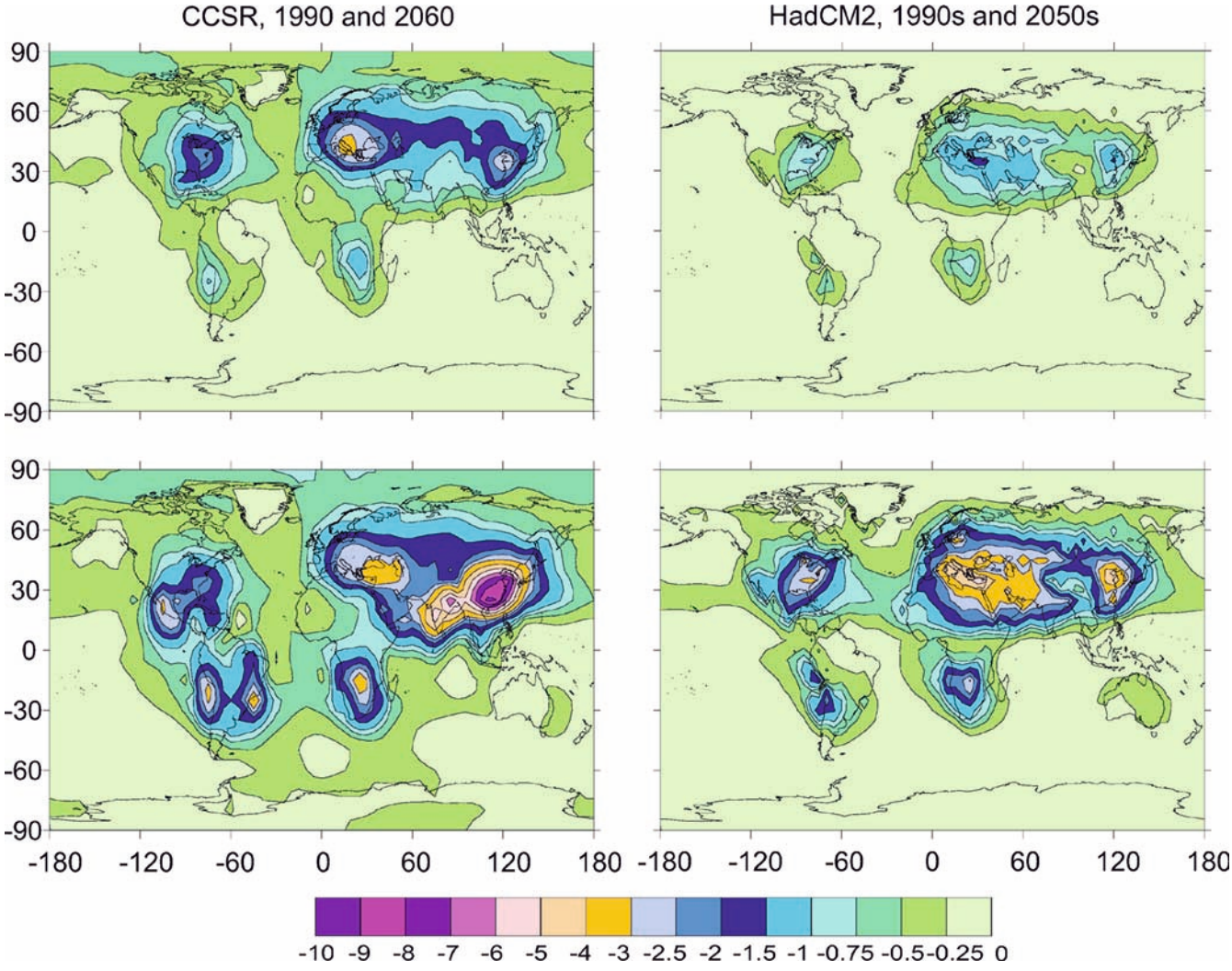

Fig. 1 Geographical variation of aerosol radiative forcing ($W\ m^{-2}$) for two different time periods as used in CCSR and HadCM2

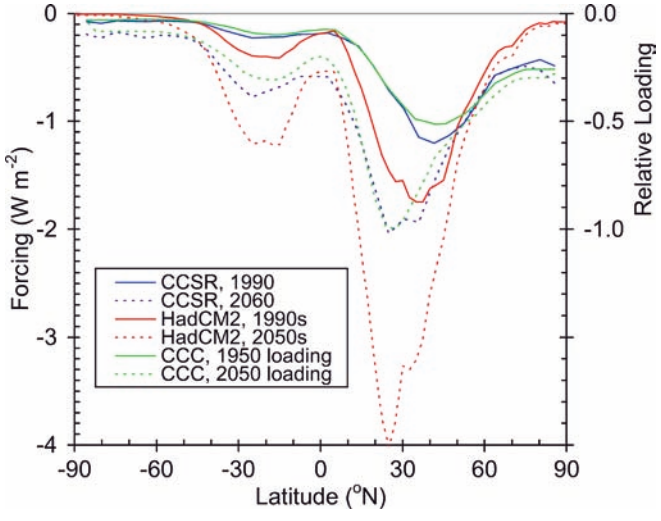

Fig. 2 Zonal-mean aerosol radiative forcing for two different time periods as used in CCSR, and HadCM2, and the variation in relative loading for CCC

compared to the observations. Conversely, the average warming closely matches the observed warming when aerosol forcing is included. By 2100, the model-predicted global-mean warming (relative to a three-decade average near 1900) ranges from 4.0 °C to 6.0 °C in the absence of aerosol forcing, and from 3.3 °C to 4.8 °C in the presence of aerosol forcing. In the CO_2-only case, all of the models except CCC cluster around a global-mean warming of about 4.0 °C by 2100, whereas CCC gives a global-mean warming of about 6.0 °C.

Figure 4 shows the ratio of average warming over land to average warming over ocean from 2000 onward for the CO_2 runs. This ratio is relatively constant over time for any given model, ranging from 1.5–2.0. The ratio for the CO_2 + aerosols runs, averaged over the last 30 years of the simulation, is within 4% of the ratio for the CO_2 runs for all models except ECHAM3 and ECHAM4, where the land/ocean warming ratio is only 90% as large. The land/sea warming ratio is reduced by up 50% at individual latitudes with large aerosol forcing

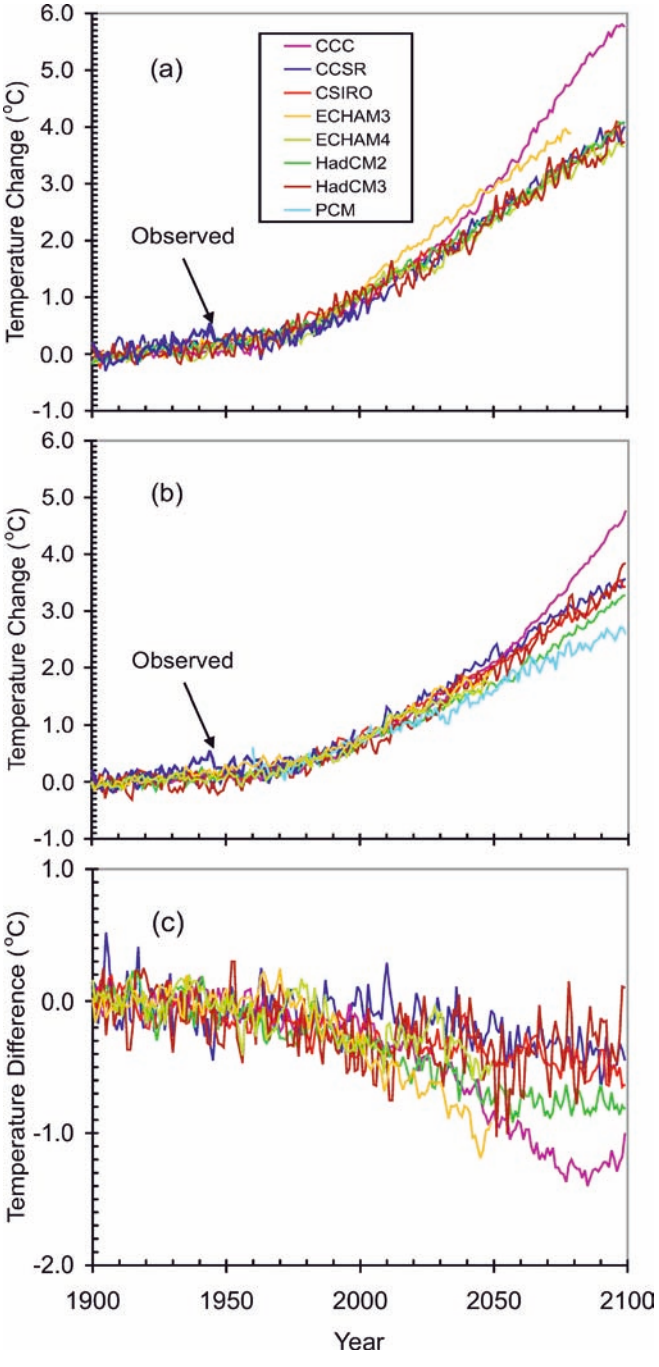

Fig. 3 Variation in global-mean surface air temperature over the period 1900–2100 as simulated by the eight AOGCMs, and comparison with the observed global-mean temperature variation over the period 1900–2002. Results are shown for (**a**) CO_2-only forcing, (**b**) CO_2 + aerosol forcing, and (**c**) the difference between the above. For the PCM, results are available only for CO_2 + aerosol forcing

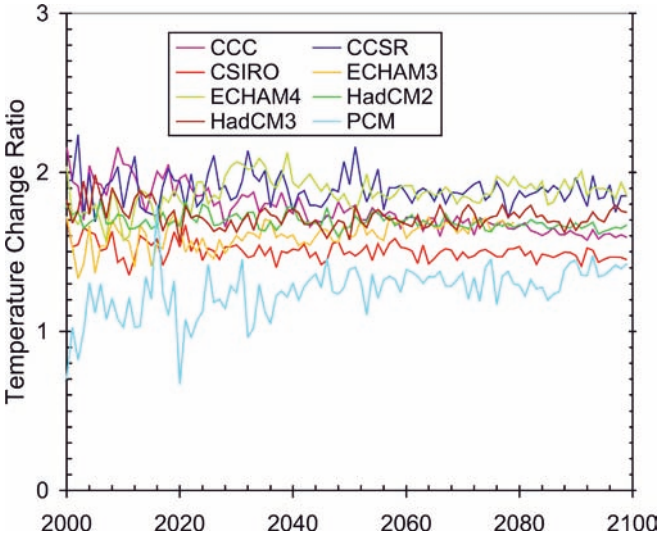

Fig. 4 Ratio of global-average warming over land to global-average warming over ocean for the CO_2 runs for all models except PCM, where results are given for the CO_2 + aerosol run

in these models. This indicates a stronger tendency for aerosols to suppress warming over land than over ocean in two of the models, but a negligible effect (relative to the noise of internally generated variability) in the other models. Regional features of the aerosol response (where present) are discussed in greater detail later.

Figure 5 compares the percentage change in global-mean, ocean-mean, and land-mean precipitation as simulated by the various models for the CO_2-only case. Three of the models (CCSR, HadCM3, and PCM) cluster around a global-mean precipitation increase of 4% by 2100, ECHAM3 experiences about a 3% increase, and the remaining models give an increase of 6–9%. Precipitation averaged over oceans increases by 1/2% (ECHAM4) to over 8% (CCC, CSIRO). Precipitation over land increases by 2% (CCC) to 11% (ECHAM3 and ECHAM4), but shows much greater interannual variability than the precipitation change over ocean. This in turn is likely due to the greater variability in the land surface warming than the ocean surface warming (not shown), thereby causing the strength of the land thermal low to oscillate and with it, the precipitation over land. In the case of CCC (Fig. 5c), land precipitation has a 50–100 year oscillation, rather than a continuous long-term upward trend, although the trend is upward by the end of the simulation.

Figure 6 directly compares the percentage change in precipitation over ocean and land for the CO_2 and CO_2 + aerosol runs, model-by-model (11-year running means are used to avoid clutter). CCC and ECHAM4 represent two extremes in the relative changes over land and over ocean: in CCC, precipitation over land is constant or decreases as the climate warms but there is a strong increase over the ocean, while in ECHAM4, there is almost no precipitation increase over ocean but one of the largest increases over land of any model. The differences in the ratio of relative precipitation increases over land and ocean cannot be explained by differences in the ratio of global-mean land to ocean warming, since there is little difference in this ratio among the various models (see Fig. 4). Similarly, differences in the ratio of land-to-ocean warming in the 30°S–30°N region (which

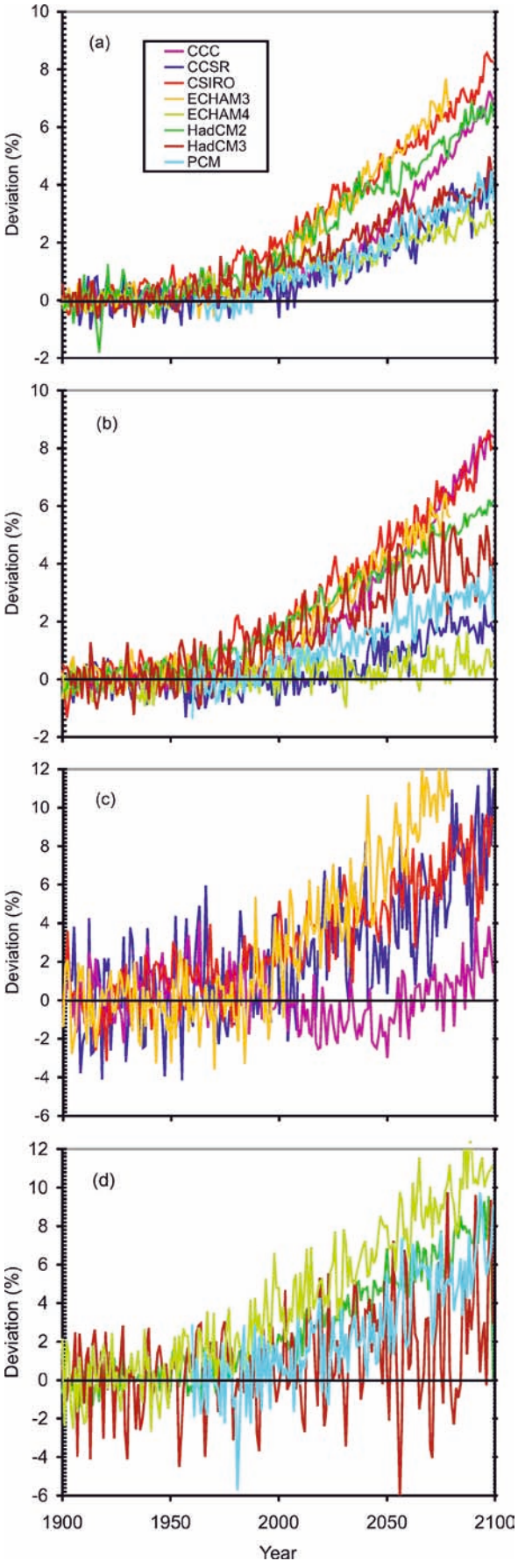

Fig. 5 Percentage change in precipitation for forcing with CO_2 averaged (**a**) globally, (**b**) over the oceans only, and (**c, d**) over land only

would dominate the global-mean precipitation) are small and not correlated with the difference in relative precipitation increase over land and ocean.

Figure 7 shows the 11-year running average of the percentage change in global mean precipitation divided by the change in global-mean temperature ($\Delta P/\Delta T$), from 2000 onward (recall: control-run trends were first removed from all model results, and ΔP and ΔT are both relative to the detrended control-run mean). Results for the CO_2 runs are shown as heavy solid lines, while results for the CO_2 + aerosol runs are shown as light dashed lines. For the CO_2 runs, the ratio converges to values ranging from 0.7%/K (ECHAM4) to about 2%/K (CSIRO and ECHAM3), indicating almost a factor a three variation in the sensitivity of global-mean precipitation to changes in global-mean temperature.

In all models the $\Delta P/\Delta T$ ratio is smaller when aerosols are included, but the difference in the ratio averaged from 2000 to the end of the simulation does not exclude zero with 95% confidence for CCC and CSIRO (taking into account auto-correlation in each time series). In ECHAM4, the $P/\Delta T$ ratio is cut roughly in half when direct aerosol forcing is added, but precipitation still increases. However, as discussed by Roeckner et al. (1999), global-mean precipitation *decreases* in this model relative to the control when indirect aerosol forcing (through changes in cloud properties) is included along with direct aerosol effects and GHG forcing.

4 Temperature response to CO_2 forcing

In this section we discuss in more detail the main features of the model temperature response to forcing by CO_2 (or due to CO_2 + aerosol forcing, in the case of PCM).

4.1 The temperature response for each AOCGM can be largely accounted for by a fixed spatial pattern (EOF_1 or $qEOF_1$) that scales up over time

Figure 8 shows temperature EOF1 for the AOGCMs for the CO_2 or (for PCM) CO_2 + aerosol runs. Figure 9 compares the fraction of the total space-time temperature variation that is accounted for by EOF1 by the different models for the CO_2 runs (and other results, discussed later). EOF1 accounts for 82% (HadCM3) to 93% (CCC) of the space-time temperature variability for the CO_2 runs. All of the model EOF1 fields display the following features: a high-amplitude amplification of the warming; greater warming over land than over the ocean at all or most latitudes; minimal warming in the North Atlantic Ocean and Labrador Sea, with a slight cooling in the later region in some cases; minimal warming or a

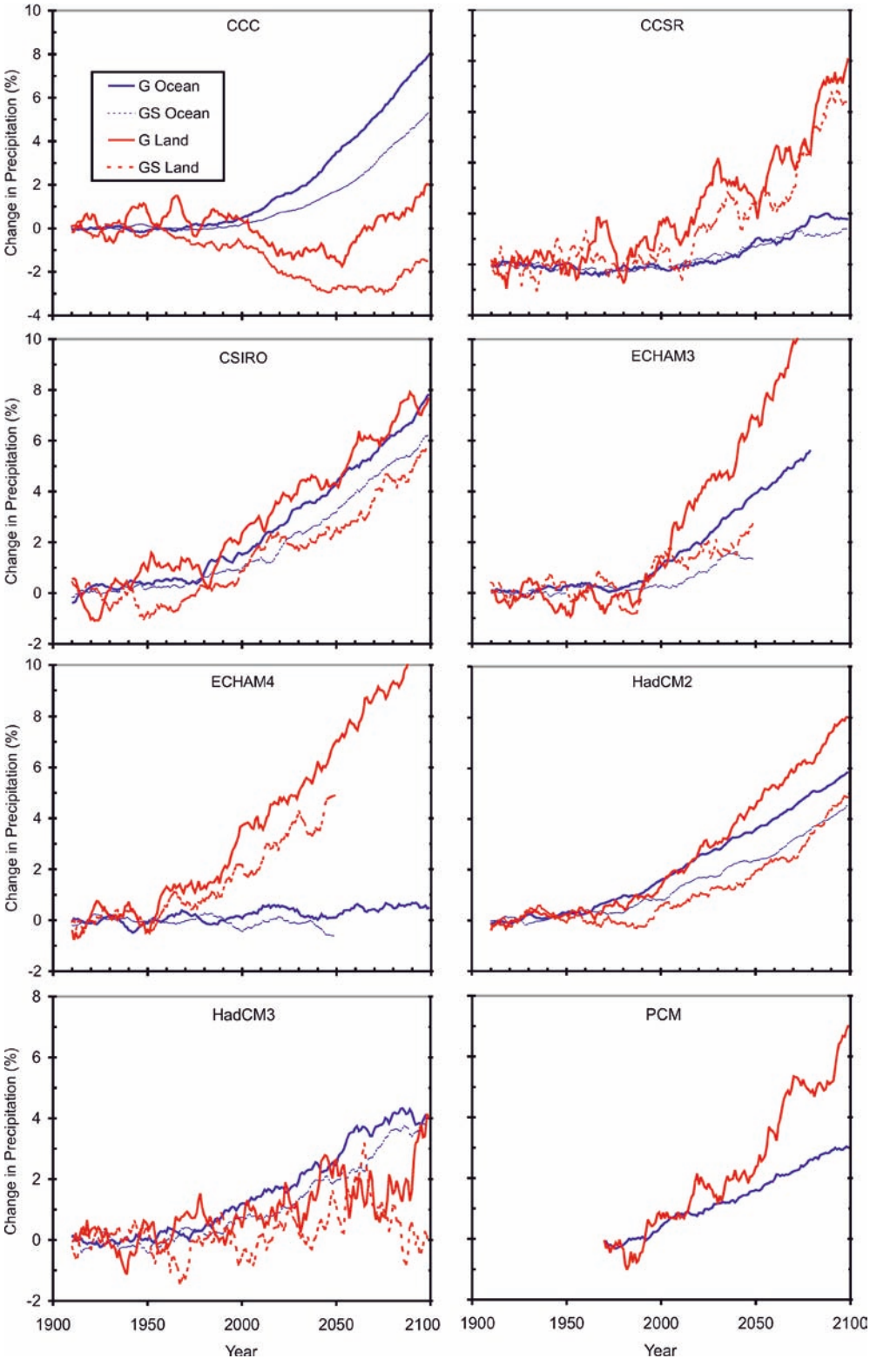

Fig. 6 Comparison of percentage change in precipitation averaged over land and ocean for the CO_2 and CO_2 + aerosol runs for each model

slight cooling in parts of the Antarctic Ocean. Regional cooling around Antarctica is most pronounced in ECHAM4, and is consistent with the temperature response maps shown for the GSD run in Roeckner et al. (1999). Many models also show greater warming in the eastern or central tropical Pacific than in the western tropical Pacific, a pattern that is similar to the deviation in tropical Pacific temperature during El Niño years.

The model EOF_1 fields for the CO_2 runs are almost perfectly correlated with the corresponding $qEOF_1$ fields ($R^2 = 0.974$ to 0.999). This confirms that EOF_1 from the CO_2 (and CO_2 + aerosol) runs is indeed picking up the

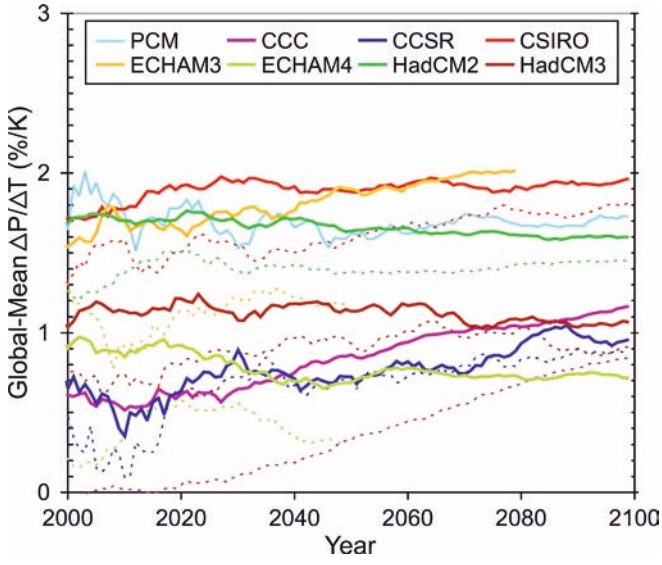

Fig. 7 Percentage change in global-mean precipitation divided by the change in global-mean temperature

global warming signal (i.e. that portion of the space-time variability that is correlated with the global-mean temperature). The EOF_1 fields are also highly correlated (R^2 = 0.22 to 0.88) with the pattern of temperature change averaged over the period 1980–2009 (referred to as $\Delta T_{1980\text{-}09}$), indicating that the long-term model temperature response structure is already well established by the 1980–2009 period. The EOF_1 fields are almost perfectly correlated (R^2 = 0.902 to 0.973) with the pattern of temperature change averaged over the last 30 years of the simulations (generally 2070–2099, referred to as $\Delta T_{2070\text{-}99}$). This reinforces the conclusion that EOF_1 is an excellent representation of the model temperature response to CO_2 forcing. The correlations are summarized in Table 3 (along with other correlations, to be discussed later). This justifies the use of EOF_1 as the signal or fingerprint to be used in spatial detection and attribution studies, as in recent work by Santer et al. (2003a,b).

4.2 Scaling EOF_1 by the global-mean temperature changes gives a close fit to the spatial temperature change on decadal and longer time scales

The local temperature change at each grid point can be estimated for each year by scaling the EOF_1 pattern such that the global-mean temperature change associated with the scaled pattern equals the model global-mean temperature change for that year. Comparison with the actual temperature change for that grid point and year gives the error associated with this scaling. Figure 10 shows the variation in the RMSE of the decadal-mean temperature change when the scaling approximation is used for the eight models, averaged over all land between 60°S and 60°N (the average RMSE was computed by weighting the square of the grid-point errors by the cosine of latitude). RMSEs of decadal-mean temperature range from 0.1 °C to 0.4 °C. There is no discernable trend in the RMSE, but the temperature change grows during the 1900–2100 period, so the relative error decreases over time. The error is due to decadal-scale internal variability in the models that is not captured by the scaling approximation. This is indicated by the fact that, in 10–43% of the land grid points (depending on the model), the largest error for any decade is no larger than one standard deviation of the 10-year means in the control run, and in only 3–25% of the grid points is the largest decadal error larger than two standard deviations (for most decades, the fraction of grid points where the error exceeds one or two standard deviations is smaller still). This is about what one would expect from chance; thus, the errors are statistically indistinguishable from zero.

Since the variability of 30-year-mean temperatures is smaller, the RMSEs of 30-year-mean temperatures are smaller (by 40–50%) than those for decadal mean temperatures. Figure 11 shows the geographic variation in the RMSE of decadal and 30-year-mean temperatures for CCSR (in which this approach works least well) and for HadCM2 (in which this approach works best). The largest errors over land occur over the interior of North America and northern Russia. In the worst case (CCSR 10-year means), the errors are no more than about 0.8 °C.

Given the similarity between EOF_1 and $\Delta T_{2070\text{–}99}$ (Table 3), an alternative is to scale $\Delta T_{2070\text{–}99}$ rather than EOF_1 by the decadal global-mean temperature change. The RMSEs (averaged over all decades between 1900–2099) using both approaches are compared in Table 4. Scaling EOF_1 gives consistently smaller errors than scaling $\Delta T_{2070\text{–}99}$, although the latter approach gives smaller errors than scaling EOF_1 toward the end of the simulation (as one would expect). Also given is the root mean square of the grid point temperature change during the last decade of the simulation. By the end of the simulation, the RMSEs are generally 5–10% of the RMS temperature change.

The approach of estimating regional climatic change by scaling GCM patterns had been used by Santer et al. (1990), Hulme et al. (1995), Hulme and Brown (1998), Mitchell et al. (1999), Schlesinger et al. (2000), Huntingford and Cox (2000), and Mitchell (2003). Mitchell et al. (1999) discuss in some detail the ability to reconstruct the time-space pattern of temperature change in HadCM2 by scaling a fixed pattern. The pattern that they use is computed the same way as our $qEOF_1$, which in turn is almost exactly the same as EOF_1. Their computed RMSEs for CO_2 and CO_2 + aerosol runs are slightly larger than those reported here for HadCM2, perhaps due to differences in the spatial averaging. Mitchell et al. (1999) note that the RMSEs using a fixed pattern based on the ensemble mean (as used here) are 2–3 times less that the RMS differences between individual members of the ensemble. They also find that the response patterns are essentially the same for slow and fast rates of growth in radiative forcing, but that the errors grow by about 50% toward the end of a stabilization scenario (rather than remaining constant).

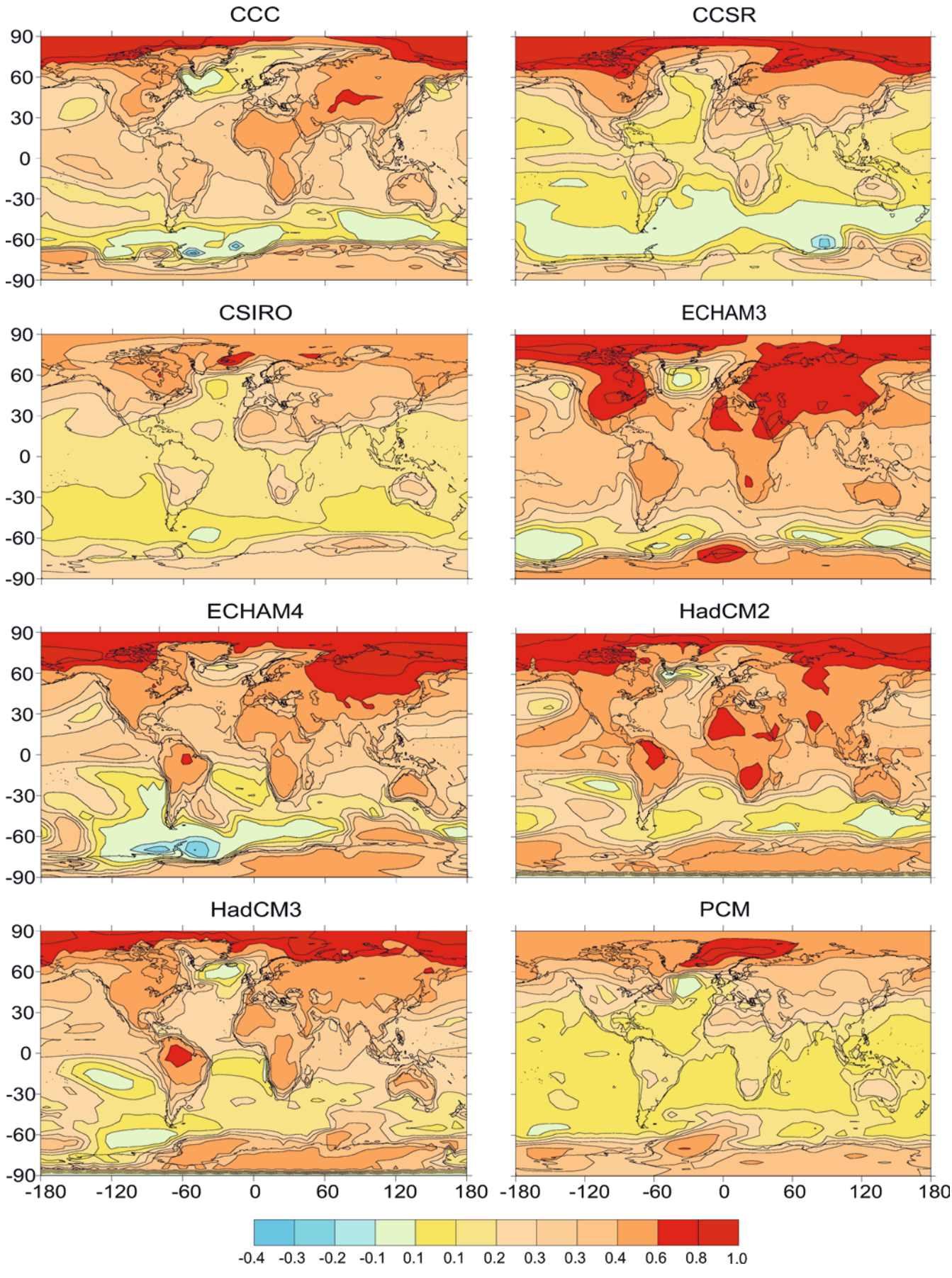
CCC
CCSR
CSIRO
ECHAM3
ECHAM4
HadCM2
HadCM3
PCM
90
60
30
0
-30
-60
-90
-180
-120
-60
0
60
120
180
-0.4
-0.3
-0.2
-0.1
0.1
0.1
0.2
0.3
0.3
0.4
0.6
0.8
1.0

◀

Fig. 8 The first temperature EOF, as computed from the CO_2 runs (all models except PCM), or as computed from the CO_2 + aerosol run (PCM)

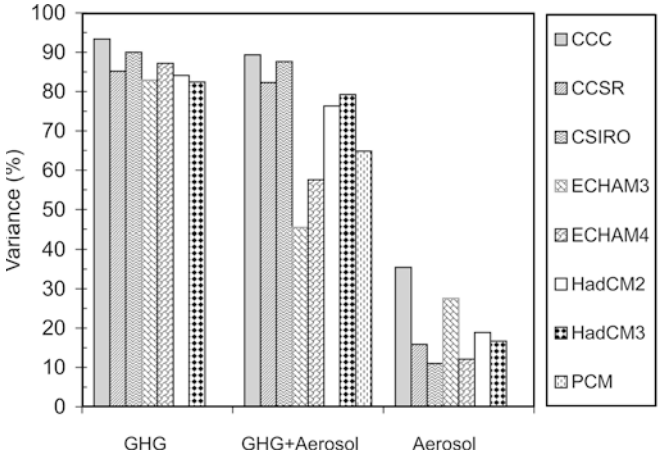

Fig. 9 The percent of the space-time temperature variability in the CO_2 runs, in the CO_2 + aerosol runs, and in the year-by-year difference between the CO_2 and CO_2 + aerosol runs that is accounted for by EOF_1

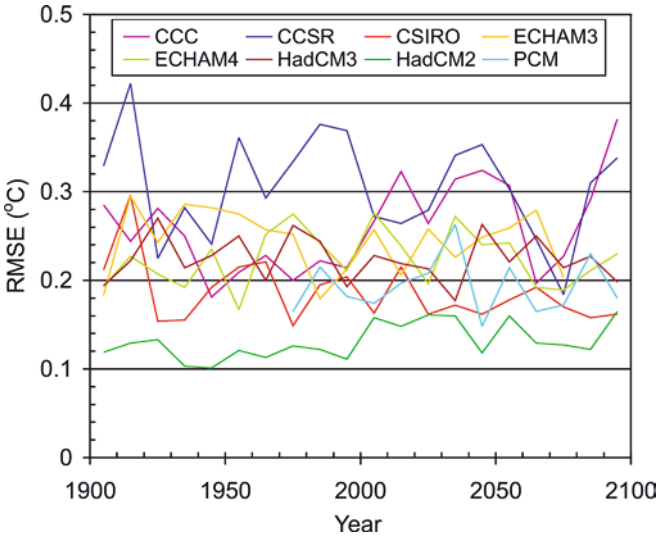

Fig. 10 Temporal variation in the mean RMSE (averaged over all land points between 60°S and 60°N) of decadal-mean surface-air temperature when the time-space CO_2 temperature response pattern is estimated by scaling annual-mean CO_2 EOF_1 by the annual global-mean temperature change

4.3 There is a high degree of similarity of the temperature-response patterns (EOF_1) among the various models

As noted, the 2D EOF_1 fields from the various models have several large-scale features in common. Figure 12 compares the latitudinal profile of the zonal-mean value of EOF_1 for the eight AOGCMs. The profiles in all cases have been scaled so that the global-mean value of the EOF field is 1.0 °C (this corresponds to a global-mean warming of 1.0 °C). All of the models show minimal warming between 40–60°S, warming close to the global-mean warming between 20°S and 40°N, and a steadily increasing warming poleward of 40°N. The maximum polar amplification falls between a factor of 2.0 and 3.0 for all the models except CCSR, which gives a poleward amplification of greater than 4.0 poleward of 80°N. Polar warming in the Northern Hemisphere is substantially greater than in the Southern Hemisphere.

Table 5 gives one-dimensional and two-dimensional common variance (R^2) between EOF_1 of the eight AOGCMs. The 1D common variances are based on the correlations between the latitudinal profiles shown in Fig. 12, while the 2D common variances are based on the 2D latitude-longitude fields. The 1D common variances range from 0.45 to 0.85, while the 2D common variances range from 0.22 to 0.71.

4.4 There is only a rough similarity between the latitudinal profile of the zonal-mean temperature change seen in the model EOF_1 and in the observed EOF_1, and the 2D spatial correlation (R^2) between model and observed EOF_1 is low (0.01 to 0.11)

Figure 12 includes the latitudinal profile of the zonal mean of EOF_1 as computed from the observed temperature variation over the period 1900–2000, and scaled to

Table 3 Common variance (R^2) between EOF_1 computed from the CO_2 runs and the $qEOF_1$, 1980–2009, and 2070–2099 average temperature change patterns (when available) from the CO_2 runs, or between EOF_1 computed from the CO_2 + aerosol runs and the $qEOF_1$, 1980–2009, and 2070–2099 temperature change pattern from the CO_2 + aerosol runs. Also given is the common variance between EOF_1 as computed for the CO_2 and the CO_2 + aerosol runs

Model	CO_2 Runs			CO_2 + Aerosol Runs			CO_2/CO_2 + Aerosol
	$qEOF_1$	$\Delta T_{1980–2009}$	$\Delta T_{2070–2099}$	$qEOF_1$	$\Delta T_{1980–2009}$	$\Delta T_{2070–2099}$	
CCC	1.00	0.64	0.99	1.00	0.59	0.99	0.97
CCSR	1.00	0.21	0.97	1.00	0.16	0.96	0.99
CSIRO	0.97	0.82	0.97	0.99	0.73	0.99	0.95
ECHAM3	1.00	0.46	0.98	0.99	0.08	0.90	0.26
ECHAM4	1.00	0.79	1.00	1.00	0.79	0.95	0.85
HadCM2	0.97	0.88	0.98	1.00	0.67	1.00	0.92
HadCM3	0.99	0.75	0.99	1.00	0.35	0.99	0.95
PCM	n/a	n/a	n/a	0.99	n/a	0.90	n/a

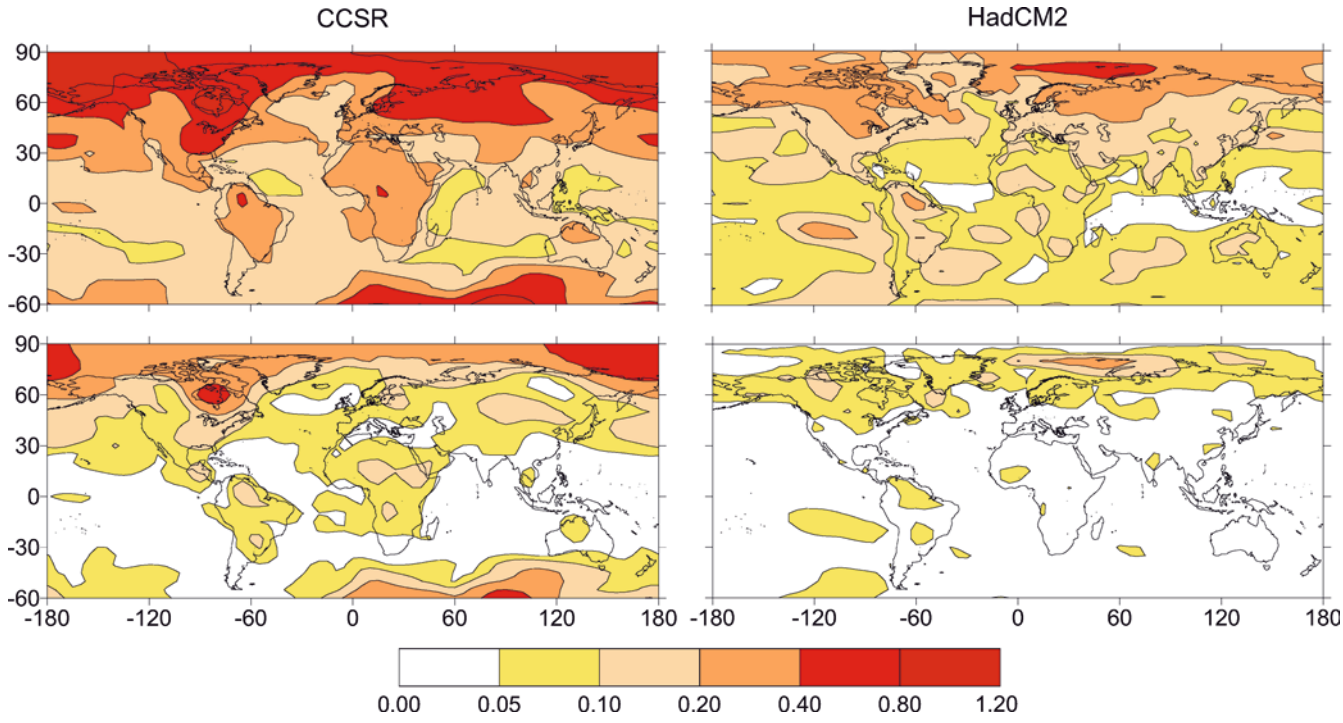

Fig. 11 Geographic variation in the RMSE of decadal-mean and 30-year-mean surface air temperature for CCSR (*left*) and HadCM2 (*right*) when annual-mean temperatures are estimated by scaling annual-mean CO_2 EOF_1 by the annual- and global-mean temperature change

a global-mean warming of 1.0 °C. Figure 13 shows the EOF_1 field as computed from the observed data. As observed data, the grid-point data available from the Climatic Research Unit at the University of East Anglia (http://www.cru.uea.ac.uk) were used. In computing the observed EOF, only grid points with 30 years or more of data were used. Zonal-mean data are shown in Fig. 12 only for latitudes where the data extend back at least 50 years with at least 50% coverage. The model EOFs pertain to the period 1900–2100 but, as noted, these EOFs are highly correlated with the warming up to 1980–2009. Thus, it is useful to compare the broad features of the model and observed EOF patterns.

Both the models and observations show smaller warming in the SH than in the NH, although the asymmetry is more pronounced in the models. In the models there is a pronounced minimum in the warming between 40–60°S which contrasts with a local maximum in the observations between 40–50°S. As well, the observed zonal-mean EOF_1 drops off poleward of 50°N rather than continuing to increase with increasing latitude, as in the models. It should also be noted that

Table 4 Root mean square error (RMSE) of the decadal-mean grid point change in temperature (K) or precipitation (mm/day) for the CO_2 runs as computed by scaling EOF_1or the 2070–2099 average change (where available) by the change in global-mean temperature, averaged over the 20 decades from 1900–2099. For PCM, results are for the CO_2 + aerosol run. For the other models, the values in brackets are the errors when CO_2 $EOF_1$is used to predict the temperature or precipitation response pattern for the CO_2 + aerosol run. Also given is the root mean square (RMS) of the decadal-mean grid-point temperature or precipitation change for the last decade of the CO_2 run (CO_2 + aerosol run in brackets for precipitation). RMSE and RMS values are averaged over land grid points only between 60° S and 60° N

Model	Temperature change (K)			Precipitation change (mm/day)		
	RMSE, scaling of EOF_1	RMSE, scaling of $\Delta T_{2070–2099}$	RMS of model grid-point changes	RMSE, scaling of EOF_1	RMSE, scaling of $\Delta P_{2070–2099}$	RMS of model grid-point changes
CCC	0.26 (0.22)	0.31 (0.25)	7.9	0.20 (0.15)	0.22 (0.18)	0.62 (0.60)
CCSR	0.31 (0.33)	0.35 (0.37)	5.5	0.22 (0.21)	0.19 (0.19)	0.59 (0.53)
CSIRO	0.19 (0.18)	0.23 (0.21)	5.1	0.10 (0.10)	0.11 (0.11)	0.40 (0.36)
ECHAM3	0.25 (0.37)	0.28 (0.36)	4.8	0.15 (0.18)	0.17 (0.17)	0.50 (0.39)
ECHAM4	0.22 (0.23)	0.28 (0.24)	5.9	0.14 (0.12)	0.15 (0.12)	0.64 (0.35)
HadCM2	0.13 (0.18)	0.21 (0.21)	5.6	0.21 (0.18)	0.20 (0.16)	0.75 (0.65)
HadCM3	0.22 (0.25)	0.29 (0.30)	5.5	0.67 (0.66)	0.19 (0.20)	0.68 (0.76)
PCM	0.21	0.23	2.7	1.26	0.15	0.32

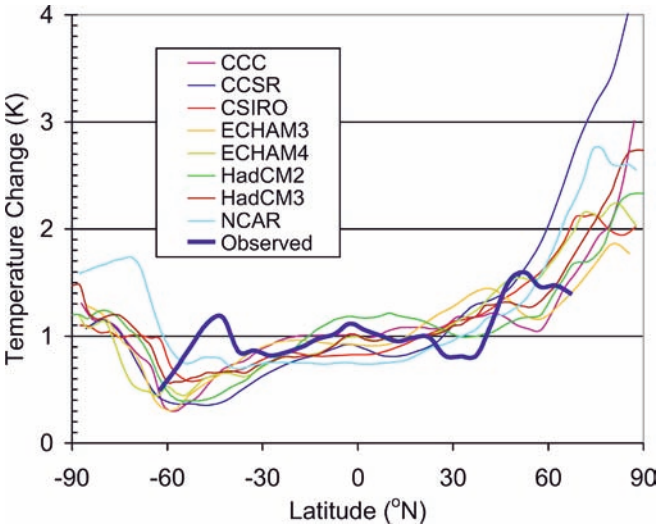

Fig. 12 Latitudinal variation in the zonal-mean temperature EOF_1 field for the eight AOGCMs (over the period 1900–2099) and for observations (over the period 1900–2000). For all except the PCM, results are for the CO_2-only runs, while for the PCM, the results pertain to the CO_2 + aerosol run

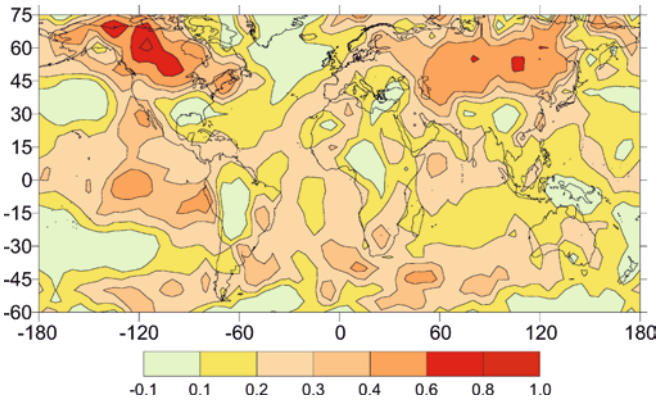

Fig. 13 The observed temperature EOF_1, computed over the period 1900–2000

alternative measures of the pattern of observed temperature change, based on $qEOF_1$ and the 100-year trend, show no hemispheric asymmetry (see Harvey and Wigley 2003, their Fig. 4). Our model-observations comparison differs from that of Kelly et al. (1999), who computed observational EOFs after first normalizing the observed temperature variations by the standard deviation at each grid point. As a result, their observed EOF_1 has a maximum at low latitudes rather than at high latitudes. Surprisingly, they concluded that this pattern contradicts the latitudinal profile of the zonal-mean temperature response to increasing CO_2 obtained by AOGCMs. Normalizing the grid-point temperature data by the standard deviation is appropriate in detection and attribution studies, but for purposes of validating the shape of the long-term trend in the model temperature response, the un-normalized data should be used (otherwise, a model that give the correct average temperature response but has higher or lower inter-annual variability than in the observations, will generate a different EOF field).

Table 6 gives the 1D and 2D common variances (R^2) between the model and observed EOF_1. Figure 13 (which shows observed EOF_1) can be compared with the model EOF_1 results given in Fig. 8. The 1D common variances range from 0.25 to 0.61. In spite of the rough agreement between model and observations in the zonal-mean EOF_1 profile, there are substantial disagreements at the regional scale (compare Figures 8 and 13). As a result, the 2D common variance between any of the models and observations is quite low, ranging from 0.01 (PCM) to 0.11 (ECHAM3), as shown in Table 6. The model EOF_1 fields agree much more with each other than with the observations. The low agreement is likely due to several factors, including: errors in the model physics, imperfect representation of sulfate aerosol forcing, neglect of other forcings (land use changes and other aerosols in particular), incomplete and imperfect observations, and internal variability in both the models and observations combined with the fact that the observations are based on changes only up to present.

Flato and Boer (2001) report that a more recent version of CCC, using isopycnal/ diapycnal rather than horizontal/vertical mixing, produces much less hemispheric asymmetry than the version shown in Fig. 12. In particular, the minimum in the warming seen at 60°S in CCC and most other models is absent in the isopycnal version of CCC. However, ECHAM4 and HadCM3 also

Table 5 Common variance (R^2) between CO_2 temperature $EOF_1$of different models. Values above the diagonal are the correlations between the latitude-longitude EOF fields, while values below the main diagonal are the correlations between the latitudinal profiles of the zonal-mean EOF fields

	CCC	CCSR	CSIRO	ECHAM3	ECHAM4	HadCM2	HadCM3	PCM
CCC		0.66	0.40	0.51	0.58	0.64	0.53	0.22
CCSR	0.48		0.65	0.56	0.67	0.68	0.71	0.48
CSIRO	0.60	0.72		0.42	0.57	0.54	0.61	0.64
ECHAM3	0.88	0.40	0.66		0.58	0.53	0.56	0.24
ECHAM4	0.74	0.76	0.89	0.77		0.63	0.65	0.29
HadCM2	0.85	0.45	0.58	0.68	0.69		0.71	0.40
HadCM3	0.82	0.76	0.85	0.78	0.93	0.78		0.55
PCM	0.20	0.71	0.65	0.20	0.47	0.22	0.51	

Table 6 Common variance (R^2) between models (with CO_2 forcing) and observations for temperature EOF_1. The first column gives the correlations between the latitudinal profiles of the zonal-mean EOF fields, while the second column gives the correlation between the latitude-longitude fields

Model	1D correlation	2D correlation
CCC	0.52	0.08
CCSR	0.28	0.08
CSIRO	0.61	0.04
ECHAM3	0.62	0.11
ECHAM4	0.62	0.09
HadCM2	0.45	0.05
HadCM3	0.54	0.04
PCM	0.25	0.01

use isopycnal/diapycnal mixing, but still display substantial hemispheric asymmetry.

5 Temperature response to aerosol forcing

In this section, the temperature response of the CO_2 + aerosol runs is analyzed. To isolate the effect of aerosol forcing on the climate model response, the difference in the annual-mean temperatures at each grid point and for each year between runs with CO_2 forcing only and with CO_2 + aerosol forcing is computed. This space-time aerosol-effect array is then subjected to the same EOF or qEOF analysis as applied to the CO_2 and CO_2 + aerosol space-time arrays. Additional measures of the effect of aerosols are also considered.

5.1 As in the CO_2 runs, the temperature response pattern to CO_2 + aerosol forcing can be largely accounted for by scaling a fixed spatial pattern that in turn is highly correlated with the CO_2 pattern in most cases

Table 3 shows the common variance (R^2) between EOF_1, qEOF1, $\Delta T_{1980\text{-}09}$, and $\Delta T_{2070\text{–}09}$ for the CO_2 + aerosol runs. As in the CO_2 runs, the EOF_1, $qEOF_1$, and $\Delta T_{2070\text{-}99}$ fields are almost perfectly correlated with each other (R^2 = 0.95–1.00). The correlation between EOF_1 and $\Delta T_{1980\text{–}09}$ is not as good as for the CO_2 runs, particularly for ECHAM3 and HadCM3. Figure 9 shows the fraction of space-time variability in the CO_2 + aerosol runs that is accounted for by EOF_1. The accounted-for variance is comparable to that accounted for by EOF_1 in the CO_2 runs, except for ECHAM3 and ECHAM4, where EOF_1 accounts for only 50–60% of the variance in the CO_2 + aerosol runs.

The EOF_1 fields computed from the CO_2 and CO_2 + aerosol runs are generally highly correlated with one another (R^2 = 0.85–0.99, as shown in the last column of Table 3). The only exception is ECHAM3, where the common variance is only 0.26. As a result, CO_2 and aerosol response patterns can be separated in ECHAM3 (Hegerl et al. 2000) but not in HadCM2 (Tett et al. 1999) and the other models studied here. This in turn implies that detection of separate CO_2 and aerosol effects on climate, by searching for model-based patterns in the observational record, will not be possible in most cases.

For models with R^2 correlations between the annual-mean CO_2 and CO_2 + aerosol EOF_1 fields of 0.95 or better, the correlations between the seasonal fields are within 1–2% of the annual-mean correlations; that is, the correlations are not noticeably worse during JJA, when the radiative forcing due to sulfate aerosols is strongest due to the strong solar insolation in the regions of largest aerosol loading. For ECHAM3 and ECHAM4, where the annual-mean correlations are 0.26 and 0.85, respectively, the correlations during JJA are 0.38 and 0.76, respectively; that is, the correlation during JJA is stronger than the annual-mean correlation in one case and weaker in the other case.

5.2 The CO_2 + aerosol spatial response can be accurately simulated by scaling the CO_2 response pattern by the global-mean warming for the CO_2 + aerosol case

Given that the primary CO_2 and CO_2 + aerosol response patterns (EOF_1) are highly correlated in most cases, and that a large part (> 80%) of the CO_2 + aerosol space-time response is accounted for by EOF_1, one would expect that the CO_2 + aerosol spatial response can be accurately simulated by scaling the CO_2 response pattern by the global- mean warming for the CO_2 + aerosol case. This expectation is confirmed by Table 4, which gives the errors (in brackets) in decadal-mean temperature using this approach. RMSEs for the CO_2 + aerosol run are generally within 10% of the errors for the CO_2 run. The most notable exception is ECHAM3. In this case the error increases by 50%, most likely due to the much poorer correlation between the CO_2 and CO_2 + aerosol EOF_1 fields than for the other models.

In their application of the scaling approach to HadCM2, Mitchell et al. (1999) found that the RMSE error for the CO_2 + aerosol case is similar to that for the CO_2 case at the start of the simulation, then grows to about twice the error for the CO_2 case by 2100. In contrast, the RMSEs for the CO_2 + aerosol cases do not systematically increase over time here, and the average errors are comparable for the CO_2 and CO_2 + aerosol runs in most models. Of course, if very large aerosol increases are assumed, such as the 10-fold increase over present emissions used by Schlesinger et al. (2000) for sensitivity testing, then one can expect important differences in the CO_2 and aerosol response patterns. Similarly, if the response pattern derived from a run with a limited range of radiative forcing is used to predict the response pattern for an AOGCM run with a much larger range of

Table 7 Common variance (R^2) between alternative measures of the effect of aerosols on temperature. EOF_1, $qEOF_1$, and $\Delta T_{2070–99}$ are based on direct analysis of the year-by-year differences between the CO_2 and CO_2 + aerosol runs

Model	EOF_1 versus $qEOF_1$	EOF_1 versus $\Delta T_{2070–99}$	$qEOF_1$ versus $\Delta T_{2070–99}$
CCC	0.99	0.93	0.92
CCSR	0.01	0.15	0.80
CSIRO	0.78	0.65	0.80
ECHAM3	0.99	0.70	0.71
ECHAM4	0.37	0.48	0.58
HadCM2	0.80	0.74	0.96
HadCM3	0.20	0.01	0.41

radiative forcings, then substantially larger errors can result, as found by Huntingford and Cox (2000). However, given that the future sulfur emissions in the IS92a scenario are now regarded as unrealistically large, it can be concluded that, for a realistic range of future CO_2 and sulfur emissions scenarios, scaling the CO_2 temperature response pattern by the net CO_2 + aerosol radiative forcing will give an accurate projection of regional temperature change patterns at decadal and longer time scales. This conclusion, and all other work using the pattern-scaling approach, is subject to the key assumption that critical thresholds are not crossed, leading, for example, to an abrupt re-organization of the oceanic circulation.

5.3 Alternative measures of the effect of aerosols on temperature often disagree with one another

The effect of aerosols on the temperature response can be represented by EOF_1 or $qEOF_1$ of the year-by-year temperature differences, or by the 30-year average of the difference in temperatures between CO_2 and CO_2 + aerosol runs. Table 7 gives the common variance (R^2) between all possible combinations of these three representations for the seven models with both CO_2 and CO_2 + aerosol results. In four models (CCC, CSIRO, ECHAM3, HadCM2), the R^2 correlations between any two fields are at least 0.65, while in the other three models, one or more pairs of fields have a substantially smaller correlation. In every case where EOF_1 and $qEOF_1$ differ from one another, $qEOF_1$ is better correlated with $\Delta T_{2070–99}$ than is EOF_1. These are the two most physically direct representations of aerosol temperature effects, so the strong correlation is not surprising.

Figure 14 compares the three representations of the effect of aerosols on temperature for CCSR, ECHAM3, ECHAM4, and HadCM3. Except for ECHAM3, results are illustrated for these models because two or more of the three representations differ strongly from one another. Results are shown for ECHAM3 because the response pattern to aerosols differs strongly from CO_2 EOF_1 using any representation, containing a consistent pattern of positive and negative temperature effects. Reasons for the differences between the various representations of the effect of aerosols on temperature are elucidated later.

5.4 The first EOF of the temperature response to aerosol forcing strongly resembles the negative of the temperature response to CO_2 forcing in some models, strongly resembles control-run EOF_1 in some models, and is a mixture of the CO_2 and control-run EOF_1 in other models.

Table 8 gives the common variance between aerosol EOF_1 and the control and CO_2 EOF_1 for each of the models. In all of the models except CCSR, ECHAM4, and HadCM3, aerosol EOF_1 is similar ($R^2 > 0.5$) to CO_2 EOF_1. The common variance is strongest for the CCC model ($R^2 = 0.77$). This result is consistent with the analysis of Reader and Boer (1998) who find, in CCC, that the temperature response pattern with CO_2 and aerosol forcing is very close to that of CO_2 alone, but scaled down in proportion to the reduced global-mean warming. This is because the spatial response pattern, with or without aerosol forcing, is governed by the regional variation in feedback processes (such as changes in the extent of ice and snow at high latitudes) and not by the spatial variation in the forcing (see Harvey 2000, Ch 3, for a quantitative analysis of this general feature of climate models). These feedbacks in turn are driven by the overall climatic warming. When aerosol forcing is added to CO_2 forcing, the overall strength of the feedbacks is reduced due to the smaller global-mean warming, but the response pattern is largely unchanged.

Conversely, aerosol EOF_1 shows almost no correlation with the aerosol forcing or loading pattern in those models where the forcing or loading pattern was available to the author (CCC, CCSR, HadCM2), as indicated by the low R^2 values given in Table 9. There is a superficial resemblance between the aerosol forcing and CO_2 EOF_1 patterns, in the sense that both the forcing and the response to CO_2 forcing are strong (or strongest) over NH mid-latitude continents, and stronger in the NH than in the SH. However, the common variance between the aerosol forcing pattern and CO_2 EOF_1 is much less (0.17–0.22; see Table 9) than between aerosol EOF_1 and CO_2 EOF_1 for the CCC and HadCM2 models.

In the case of CCSR and HadCM3, aerosol EOF_1 shows no resemblance to either CO_2 EOF_1 or to the spatial pattern of aerosol radiative forcing. Indeed, aerosol EOF_1 in CCSR and, to a lesser extent, HadCM3, contains adjacent regions of strong warming and cooling effects, even though the radiative effect of aerosols is cooling everywhere. In these models, the aerosol EOF_1 pattern closely resembles control-run EOF_1 (see Harvey and Wigley 2003), and this is reflected in the high

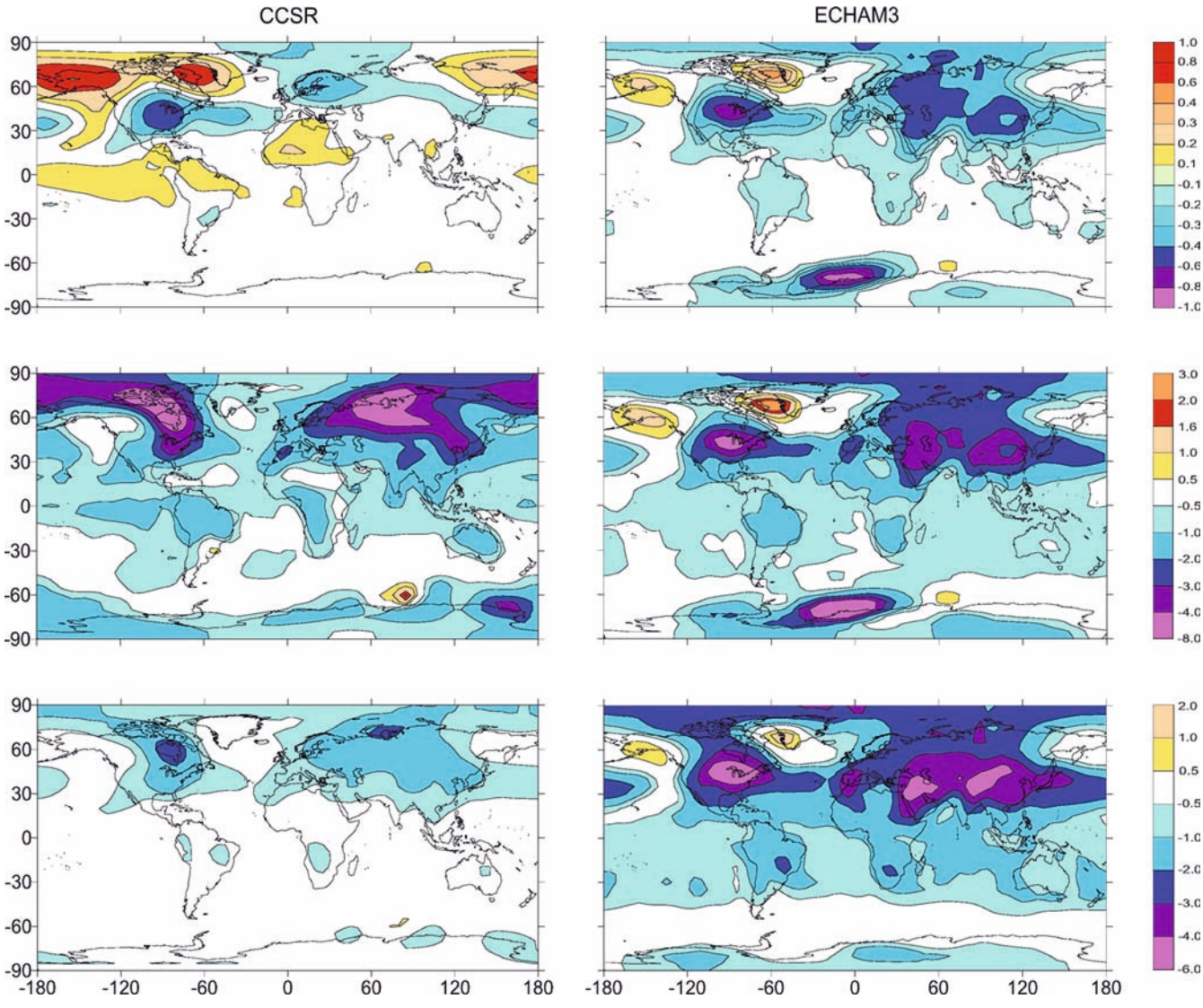

Fig. 14a Comparison of three measures of the effect of aerosols on temperature (EOF_1, $qEOF_1$, and $\Delta T_{2070–99}$, as the *top*, *middle*, and *lower row*, respectively) for CCSR, ECHAM3, ECHAM4, and HadCM3. For ECHAM3 and ECHAM4, $\Delta T_{2040–49}$ is shown

common variance (R^2 = 0.75–0.87) between aerosol EOF_1 and control EOF_1 seen in Table 8. Conversely, the correlation between aerosol and control-run EOF_1 is smallest in CCC. CCC and CCSR thus represent two extremes in the first EOF of the climate model response to aerosol forcing: aerosol EOF_1 can resemble the response to CO_2 forcing alone (giving a high correlation with CO_2 EOF_1 but a small correlation with control EOF_1), or can resemble the control-run variability (giving a high correlation with control EOF_1 but a small correlation with CO_2 EOF_1). ECHAM3 shows modest correlation between aerosol and CO_2 EOF_1 but no correlation between aerosol and control EOF_1. The other climate models involve varying combinations of these two responses, as indicated by the common variances given in Table 8.

It is not surprising that at least part of aerosol EOF_1 should resemble the pattern of control-run variability. This is because the control-run variability is superimposed on both the CO_2 and CO_2 + aerosol runs. The year-to-year deviations in the temperature patterns for both the CO_2 and CO_2 + aerosol runs will thus resemble the pattern of control-run variability, so the year-by-year differences between the two cases will also resemble the control-run variability pattern. This implies that this component of the aerosol response is noise. This is confirmed by Fig. 15, which shows the time series of the amplitude for aerosol EOF_1 (and EOF_2, discussed later) for the seven models. In the two models where EOF_1 most strongly resembles control-run EOF_1, there is no long-term trend in the amplitude of EOF_1. However, there is a long-term trend in the amplitude of aerosol EOF_1 in the four models (CCC, CSIRO, ECHAM3, and HadCM2) where EOF_1 has the strongest resemblance to CO_2-run EOF_1.

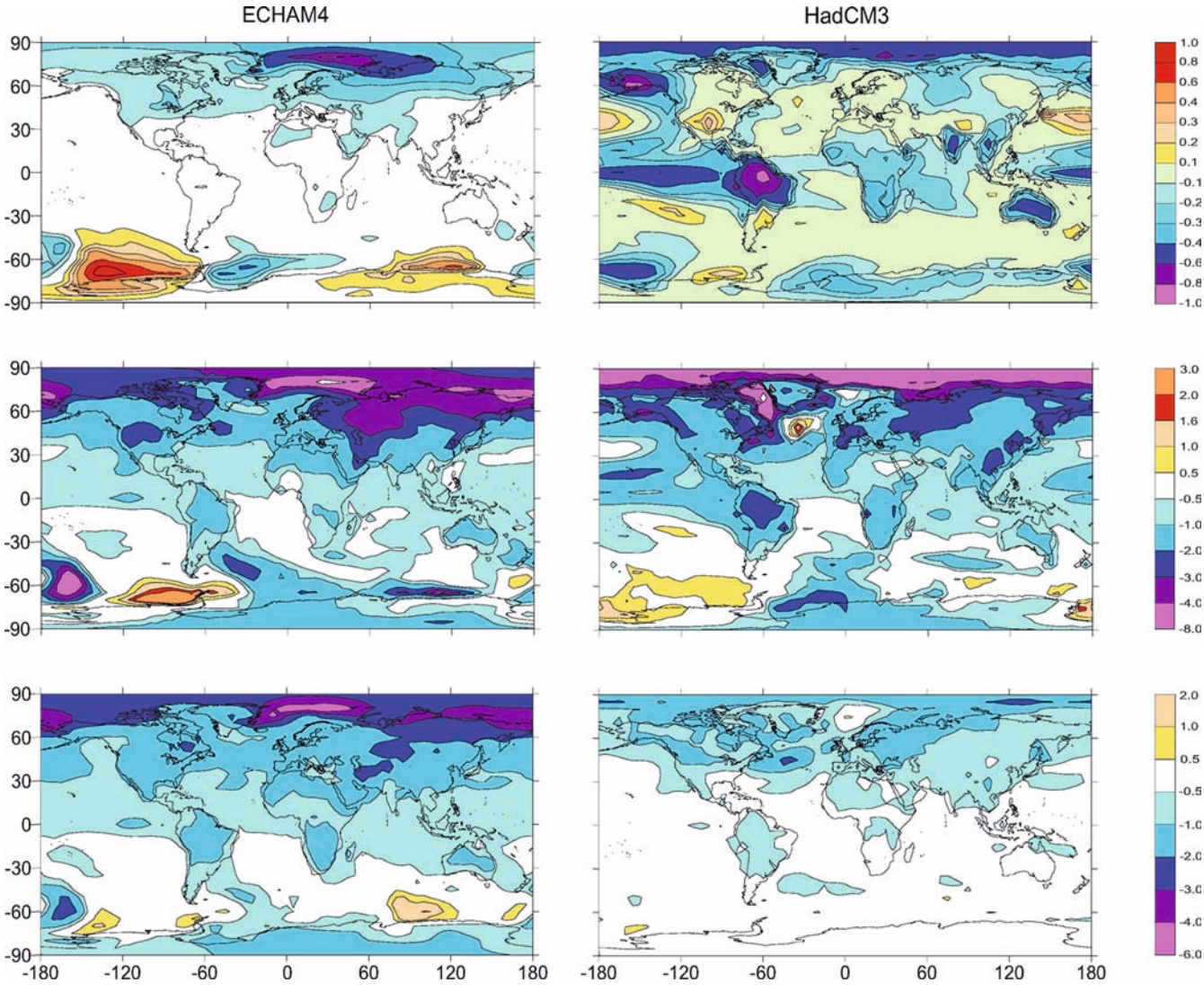

Fig. 14b (Contd)

Table 8 Common variance (R^2) between aerosol-temperature-effect EOF_1or EOF_1 ($aEOF_1$and $aEOF_2$) and control-run EOF_1($cEOF_1$) and CO_2 -run EOF_1($gEOF_1$), and between aerosol quasi-EOF_1($aqEOF_1$) and CO_2 -run quasi-EOF_1($gqEOF_1$). Also given is the percent of the space-time variation in the aerosol effect that is explained by aerosol EOF_1, EOF_2, and $qEOF_1$

Model	Common variance between $aEOF_1$and:		Common variance between $aEOF_2$ and:		Common variance between $aqEOF_1$and:	Percent explained variance		
	$cEOF_1$	$gEOF_1$	$cEOF_1$	$gEOF_1$	$gqEOF_1$	$aEOF_1$	$aEOF_2$	$aqEOF_1$
CCC	0.10	0.77	0.83	0.03	0.75	34.7	5.4	46.8
CCSR	0.87	0.01	0.08	0.43	0.57	15.9	8.5	4.3
CSIRO	0.17	0.56	0.14	0.00	0.61	11.0	7.9	9.0
ECHAM3	0.00	0.54	0.03	0.00	0.58	27.5	6.8	25.6
ECHAM4	0.40	0.22	0.02	0.10	0.48	12.1	9.3	8.0
HadCM2	0.43	0.75	0.69	0.00	0.76	19.2	9.3	39.7
HadCM3	0.75	0.18	0.23	0.16	0.45	16.3	7.4	7.7

The fraction of the aerosol response that is accounted for by EOF_1 is quite small (generally less than 20%), particularly when EOF_1 resembles the control-run variability (see Fig. 9). This is consistent with the interpretation of EOF_1 in this case as noise. In the CCC model, where the aerosol response strongly resembles the CO_2 response pattern, aerosol EOF_1 accounts for 35% of the space-time variation in the aerosol effect.

Table 9 Common variance (R^2) between aerosol temperature EOF_1, aerosol EOF_1, or CO_2 $EOF_1$and the aerosol forcing pattern (CCSR and HadCM2) or loading pattern (CCC). The early patterns pertain to 1950, 1990, and 1950–79 for CCC, CCSR, and HadCM2, respectively, while the later patterns pertain to 2050, 2060, and 2040–69, respectively

Model	Common variance between early aerosol forcing pattern and			Common variance between later aerosol forcing pattern and		
	$aEOF_1$	$aEOF_1$	$gEOF_1$	$AEOF_1$	$aEOF_1$	$gEOF_1$
CCC	0.08	0.21	0.22	0.02	0.07	0.15
CCSR	0.02	0.20	0.20	0.05	0.04	0.06
HadCM2	0.14	0.16	0.17	0.21	0.06	0.17

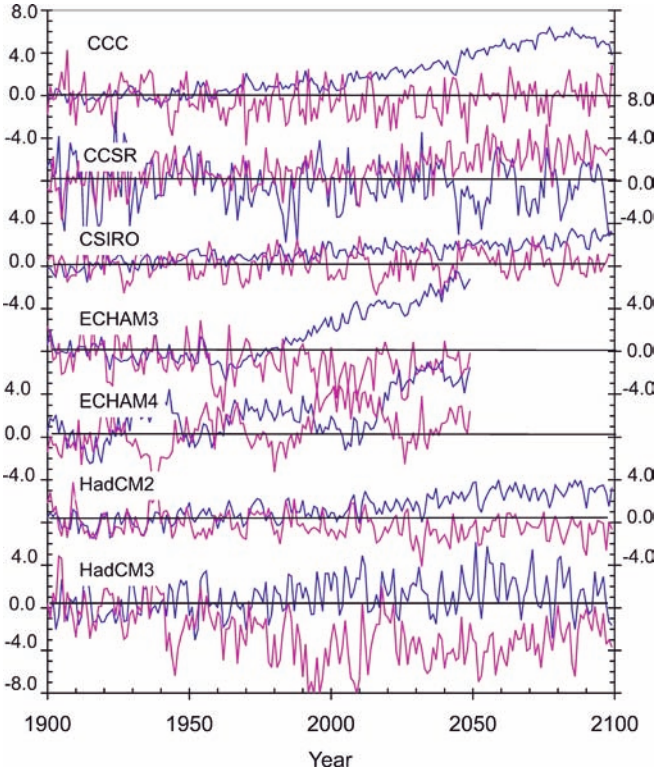

Fig. 15 Variation in the amplitude (K) of temperature aerosol-effect EOF_1 (*blue*) and EOF_2 (*pink*) for seven models

5.5 When aerosol EOF_1 is strongly correlated with control-run EOF_1, aerosol EOF_2 is modestly correlated with CO_2-run EOF_1

Common variances between aerosol EOF_1 and both control-run EOF_1 and CO_2-run EOF_1 are given in Table 8. In the models where there is a large R^2 between aerosol EOF_1 and control EOF_1 but a small R^2 between aerosol EOF_2 and CO_2 EOF_1 (CCSR and HadCM3), there is a relatively large R^2 between aerosol EOF_2 and CO_2 EOF_1. In these models the aerosol effect is weakest (see Fig. 3) and is weaker than the noise component derived from control-run EOF_1, so the aerosol effect appears as EOF_1 rather than as EOF_1. Not surprisingly, the aerosol EOF amplitude to show a long-term trend is that EOF which is most strongly correlated with the CO_2 response pattern, whether this be EOF_1 or EOF_2 (see Fig. 15).

5.6 Aerosol $qEOF_1$, which is constrained to capture the long-term temperature effect, is always moderately to highly correlated (R^2 = 0.48–0.75) with CO_2 $qEOF_1$

As explained, the first qEOF of the space-time temperature variation is computed from the correlation of the grid-point temperature with the global-mean temperature. The first aerosol qEOF will therefore give that portion of the local aerosol temperature effect that is associated with the global-mean aerosol temperature effect. Aerosol $qEOF_1$ should therefore represent the aerosol signal, with local noise removed. In contrast, both EOF_1 and EOF_2 contain a mixture of signal and noise. The common variance (R^2) with CO_2 $qEOF_1$ (which is essentially the same as CO_2 EOF_1) ranges from 0.48 to 0.76, and is always comparable to or greater than the aerosol-CO_2 EOF_1 correlation (Table 8). The percent of the space-time variation in the aerosol effect that is accounted for by aerosol $qEOF_1$ is given in Table 8. In two models (CCC and HadCM2), aerosol $qEOF_1$ accounts for almost half of the time-space variation, in ECHAM3 it accounts for about 25%, and in the other models it accounts for very little of the variation (no more than 10%). The ranking of the models in terms of the fraction of the space-time variation accounted for by $qEOF_1$ closely follows the ranking in terms of the magnitude of the global-mean aerosol temperature effect. That is, in models where the global-mean effect of aerosols in temperature is smallest (CCSR and HadCM3), $qEOF_1$ (which is related to the global-mean effect) is relatively small compared to noise, and so accounts for the smallest fraction of the variance. Where the global-mean aerosol effect is largest (CCC), $qEOF_1$ accounts for the largest fraction of the variance.

Using $qEOF_1$ instead of EOF_1, the extent of local aerosol warming effects is greatly reduced in CCSR, ECHAM4, and HadCM3 (see Fig. 14, middle row). In these models, warming due to aerosols is found only in those regions where cooling in response to CO_2 is found (i.e. at various locations around Antarctica). To the extent that this cooling is driven by global-scale changes associated with global-scale warming, it will be smaller in the presence of aerosols (i.e. the local aerosol effect is one of warming). Roeckner et al. (1999) noted the warming effect of aerosols around Antarctica in ECHAM4, but regarded it as an artifact of model vari-

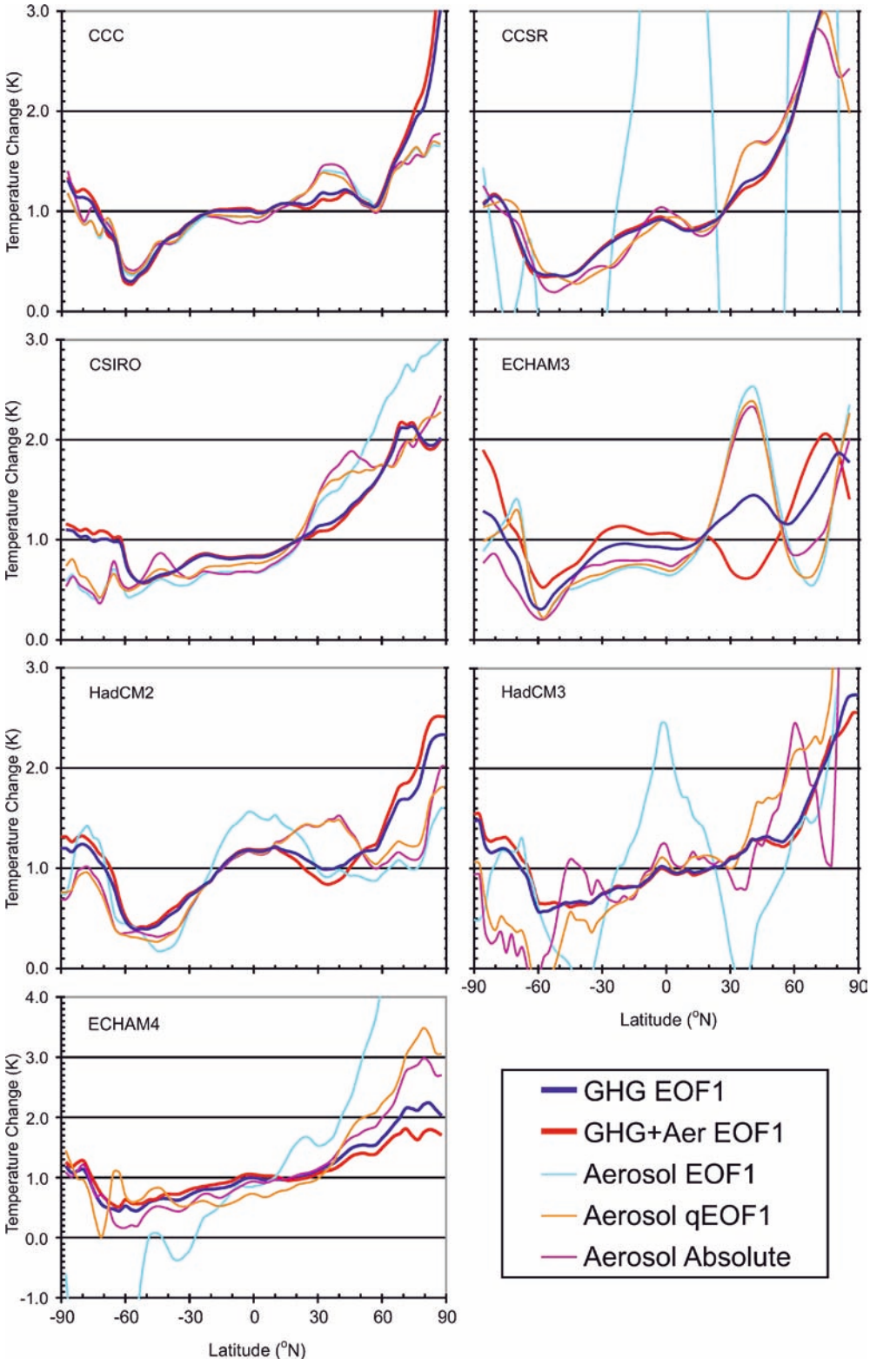

Fig. 16 Comparison of the latitudinal profiles of zonal-mean CO_2, CO_2 + aerosol, and aerosol temperature EOF_1, and of aerosol $qEOF_1$ and $\Delta T_{2070\text{-}99}$ ($\Delta T_{2040\text{–}49}$ for ECHAM3 and ECHAM4), in all cases normalized to give a global-mean value of 1 K (this makes the sign of the aerosol effects positive, which permits direct comparison with CO_2 and CO_2 + aerosol EOF_1)

ability. However, this explanation need be invoked only in the case of ECHAM3. Even here, one of the two areas of local warming due to aerosols coincides closely with a region (the North Atlantic Ocean) that experiences cooling due to CO_2 alone.

Nevertheless, it is also possible that aerosol $qEOF_1$ also contains a component of natural variability. Aerosol $qEOF_1$ is picking up regional temperature changes that are associated with differences in the global-mean temperature between the CO_2 and CO_2

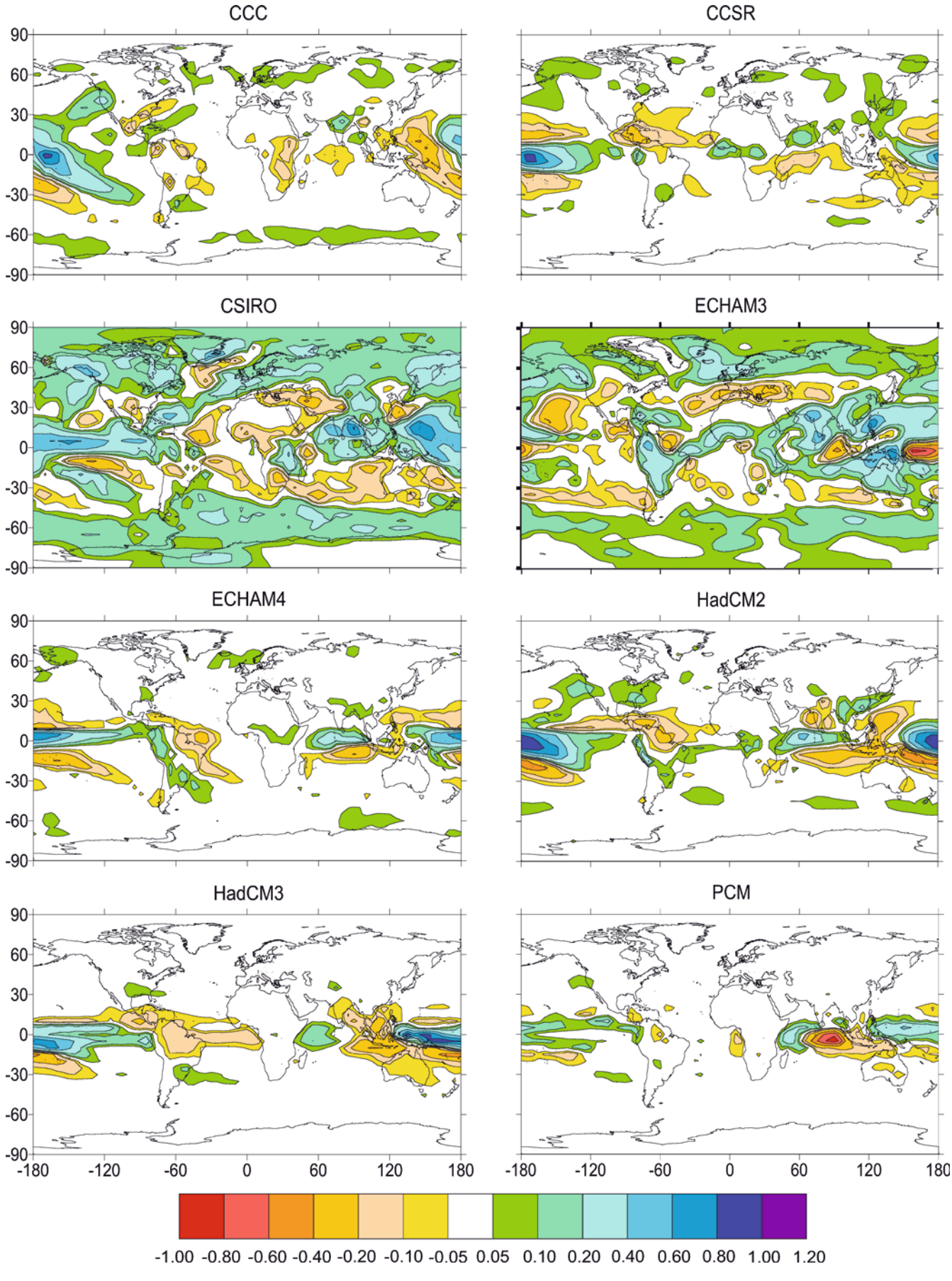
CCC
CCSR
CSIRO
ECHAM3
ECHAM4
HadCM2
HadCM3
PCM
90
60
30
0
-30
-60
-90
-180
-120
-60
0
60
120
180
-1.00 -0.80 -0.60 -0.40 -0.20 -0.10 -0.05 0.05 0.10 0.20 0.40 0.60 0.80 1.00 1.20

◀

Fig. 17 The first precipitation EOF as computed from the CO_2-only runs in all models except PCM. For PCM, the results pertain to the CO_2 + aerosol run

CO_2 + aerosol runs. If the primary mode(s) of model internal variability are associated with differences in the global-mean temperature, and the yearly amplitudes of these modes differ between the CO_2 and CO_2 + aerosol runs, then aerosol $qEOF_1$ will contain a component of model internal variability. However, the difference in temperature between CO_2 and CO_2 + aerosol runs, averaged over the period 2070–2099 (Fig. 14, lower row), shows substantial warming in response to aerosols in much the same regions as indicated by $qEOF_1$. Thus, it can be concluded that regional warming is likely to be a real response to the effect of aerosols in some models.

Regional warming can be explained as a result of changes in winds and/or ocean currents induced by the aerosols and in cloudiness, in the same way that regional cooling in response to increasing CO_2 can be explained. Qian and Giorgi (1999), using a regional climate model interactively coupled to a sulfate aerosol model, found that the direct effect of aerosols can be one of warming in places, due to a reduction in cloudiness. In all of the models studied here except ECHAM4, however, the aerosol field and climate are not interactive, that is, the changes in winds and cloudiness induced by the aerosols do not feed back onto the aerosol distribution.

5.7 Inclusion of aerosol radiative forcing has a negligible effect on the profile of zonal-mean warming and in the difference between NH and SH warming in most models, when normalized by the global-mean warming

Figure 16 shows the latitudinal variation in zonal-mean EOF_1 for the CO_2 and CO_2 + aerosol runs, as well as for aerosol EOF_1 and $qEOF_1$ and for the temperature difference between CO_2 and CO_2 + aerosol runs during the last 30 years of the CO_2 + aerosol simulation, all normalized to give a global-mean response of 1 K (this makes the aerosol curves positive rather than negative).

In light of the strong hemispheric asymmetry in the aerosol radiative forcing seen in Fig. 2, one might expect that the inclusion of aerosol radiative forcing would suppress NH warming relative to SH warming. In the CO_2-only runs, the NH warms substantially faster than the SH, due in part to the greater lag effect of the oceans in the SH and to the fact that the climate sensitivity over land is greater than over the ocean. To the extent that the inclusion of aerosols reduces the overall warming, it will also reduce the absolute difference in NH and SH warming. However, as shown in Fig. 16, the inclusion of aerosol forcing reduces the NH-SH difference only very slightly, if at all, when normalized by the global-mean warming. This is consistent with our earlier finding that the spatial pattern of climatic warming is not significantly affected by the inclusion of aerosol forcing.

The lack of a strong impact of aerosols on the NH-SH temperature difference could be an artifact of the strong hemispheric asymmetry in the temperature response in the CO_2 runs, an asymmetry that is in phase with the aerosol forcing. This asymmetry seems to be stronger than in the observations (see Harvey and Wigley 2003, their Fig. 4), so it and the lack of aerosol impact on the NH-SH temperature differential may not be realistic.

The most pronounced effect of aerosols occurs in ECHAM3, in which the warming is strongly suppressed in a band centered at 35°N. This suppression is largely over land, unlike some other models (see Fig. 14), so the net effect of aerosols in ECHAM3 is to largely eliminate the land-sea difference in warming at mid-latitudes, a point also made by Räisänen (1997). Aerosols in ECHAM3 also show one of the strongest suppressions of the increase in precipitation over land (Fig. 6) and one of the clearest suppressions of Asian monsoon rainfall (discussed later). ECHAM3 is the only model where absolute annual-mean cooling in response to the combined effects of CO_2 and aerosols occurs in some regions that warm under the influence of CO_2 alone. This is consistent with the unusually low correlation between the CO_2 and CO_2 + aerosol EOF_1 fields for ECHAM3 (Table 3).

In ECHAM4, aerosols have the strongest effect at high NH latitudes, outside the region of strongest aerosol forcing. That is, rather than uniformly reducing the warming seen from increasing CO_2 by reducing the climate feedbacks everywhere by the same proportion (as in CCC, for example), aerosols have a disproportionately large effect on the local climate feedbacks at high NH latitudes in ECHAM4.

6 Precipitation response to CO_2 and aerosol forcing

The precipitation response to both CO_2 and aerosol forcing is considerably noisier than the temperature response, and is more closely related to the primary mode of variability in the control run. As discussed in Harvey (2003), the first precipitation EOF of the control run consists of an east-west shift in the position of the precipitation maximum in the western equatorial Pacific Ocean and is associated, to some extent, with the El Niño-Southern Oscillation (ENSO). Table 10 gives the fraction of total space-time variation in annual-mean precipitation for the control and CO_2 runs, and of the year-by-year difference between the CO_2 and CO_2 + aerosol runs, that is accounted for by EOF_1 and by the first quasi-EOF, while Table 11 gives the pattern correlation between various control, CO_2, and aerosol-effect EOFs and qEOFs. Figures 17 and 18 show the first CO_2 EOF and qEOF, respectively, for each model, while Fig. 19 shows the time variation in the amplitude of the first two EOFs for the CO_2 run.

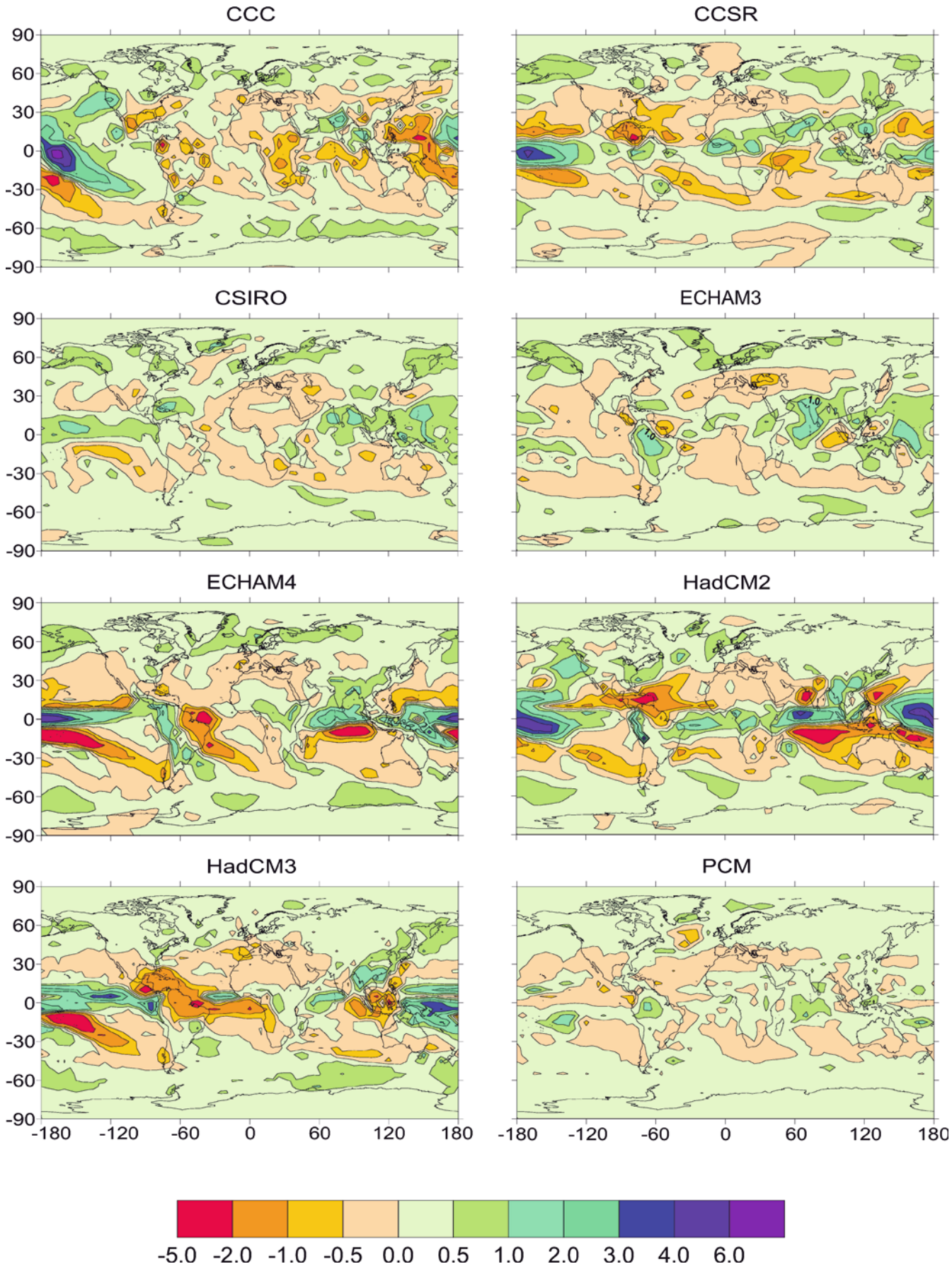
CCC
CCSR
CSIRO
ECHAM3
ECHAM4
HadCM2
HadCM3
PCM
90
60
30
0
-30
-60
-90
-180
-120
-60
0
60
120
180
-5.0
-2.0
-1.0
-0.5
0.0
0.5
1.0
2.0
3.0
4.0
6.0

◀

Fig. 18 The change in precipitation (mm/day) over the period 2070–2099 (2070–79 for ECHAM3) compared to 1890–1919 for the CO_2 runs (for PCM, changes are relative to 1960–1989 and are for the CO_2 + aerosol run)

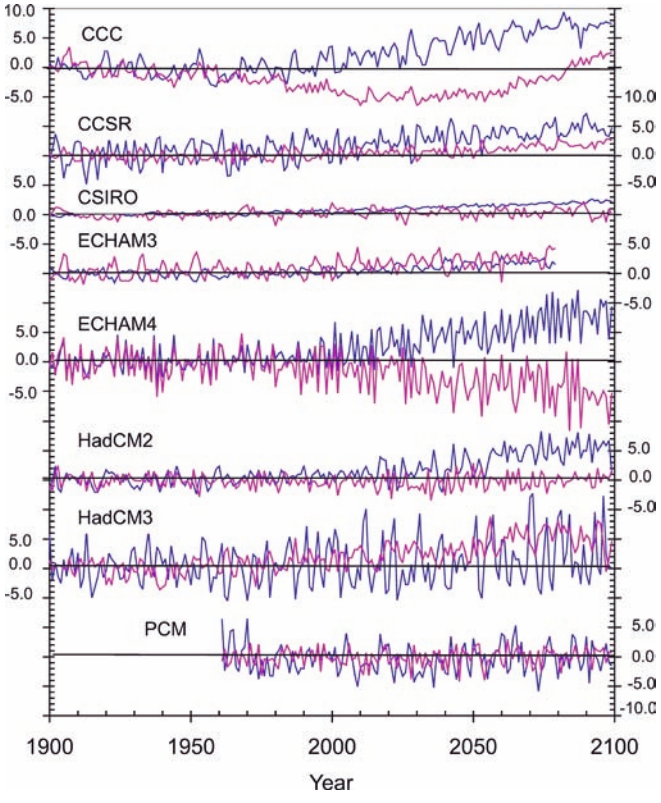

Fig. 19 Variation in the amplitude (mm/day) of precipitation EOF_1 (*blue*) and EOF_2 (*pink*) for the CO_2-only runs of all models except PCM. For PCM, the results pertain to the CO_2 + aerosol run

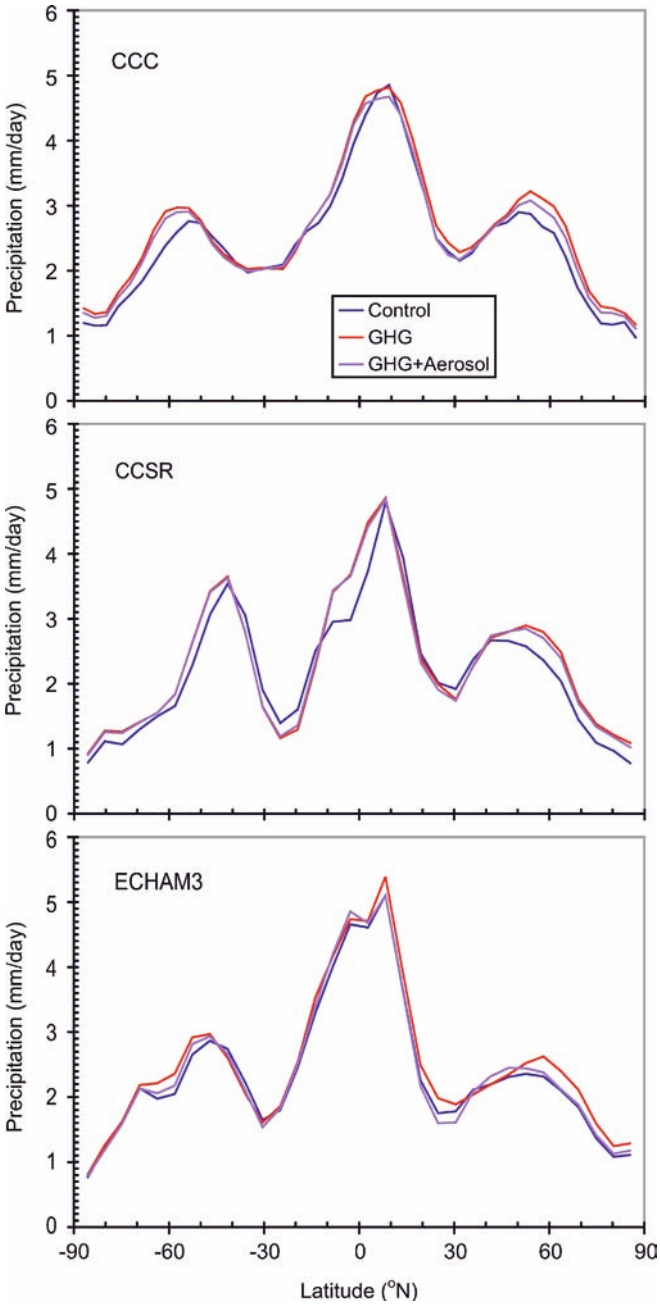

Fig. 20 Variation in zonal-mean precipitation (mm/day) for the control run, CO_2 run, and CO_2 + aerosol run for CCC, CCSR, and ECHAM3

6.1 Precipitation response patterns

The first EOF accounts for 10–26% of the global space-time control-run precipitation variability in the eight models, and always accounts for a comparable or greater fraction of total variability in the CO_2 run. In most models (CCC, CCSR, CSIRO, ECHAM4, HadCM2) the greater variance accounted for by EOF_1 in the CO_2 runs is associated with a long term increase in the amplitude of EOF_1, as seen in Fig. 19. Since CO_2 EOF_1 is generally highly correlated with control EOF_1 (Table 11, Column A), in these models the positive phase of the primary mode of control-run variability increases in importance as the climate warms. The primary mode of control-run variability is similar to the observed ENSO in most models; thus, these models show a weak tendency for the precipitation field to become more ENSO-like as the climate warms. In HadCM3, however, the greater variance accounted for by EOF_1 in the CO_2 run is associated with an increase in the year-to-year variation in the amplitude of EOF_1 rather than a long-term trend.

As seen from Fig. 18, a clear global-scale El Niño pattern (precipitation increases in the central to eastern equatorial Pacific and along the west coast of the USA, with decreases over northeastern Brazil and at least parts of northern Australia, the Philippines, and Indonesia) is seen only for CCC, HadCM2, and HadCM3. The El Niño-like precipitation response in CCC is discussed in some detail by Yu and Boer (2002). CCSR gives a precipitation increase in the central equatorial

Table 10 Percent of total-space time variability in annual-mean precipitation in the control and CO_2 runs, and in the year-by-year difference between CO_2 and CO_2 + aerosol runs, that is accounted for by the first EOF and the first qEOF. Prefixes "c", "g", and "a" refer to control, CO_2, and CO_2 + aerosol minus CO_2 runs, respectively

Model	Percent of variance				
	Precipitation EOFs			Precipitation qEOFs	
	$cEOF_1$	$gEOF_1$	$aEOF_1$	$gqEOF_1$	$aqEOF_1$
CCC	11.9	25.0	10.3	19.0	2.0
CCSR	18.7	23.2	20.6	15.1	0.8
CSIRO	10.8	13.8	9.5	13.2	0.7
ECHAM3	9.5	9.1	9.4	8.1	2.9
ECHAM4	16.9	24.0	20.8	17.8	0.8
HadCM2	22.9	30.8	24.8	39.5	5.3
HadCM3	26.0	28.9	31.4	11.5	0.8
PCM	11.5	10.9	n/a	2.8	n/a

Table 11 Precipitation results: Common variance (R^2) between various control, CO_2, and aerosol precipitation fields. The prefixes "c", "g", and "a" designate control, CO_2, and aerosol-effect fields, respectively. $g\Delta P_{2070–99}$ and $a\Delta P_{2070–99}$ are changes from 1890–1919 to 2070–2099 for the CO_2 and CO_2 + aerosol minus CO_2 runs, respectively (except for ECHAM3 and ECHAM4, where 2040–69 is used for the CO_2 run and 2040–49 is used for the aerosol run)

Model	$cEOF_1$ versus		$gEOF_1$ versus		$gqEOF_1$ versus $g\Delta P_{2070–99}$	$aEOF_1$ versus				$aqEOF_1$ versus $a\Delta P_{2070–99}$	$a\Delta P_{2070–99}$ versus $g\Delta P_{2070–99}$
	$gEOF_1$ A	$gEOF_2$ B	$gqEOF_1$ C	$g\Delta P_{2070–99}$ D	E	$cEOF_1$ F	$gEOF_1$ G	$aqEOF_1$ H	$a\Delta P_{2070–99}$ I	J	K
CCC	0.45	0.44	0.96	0.93	0.98	0.80	0.71	0.10	0.12	0.87	0.00
CCSR	0.66	0.26	0.64	0.73	0.97	0.91	0.73	0.22	0.03	0.22	0.15
CSIRO	0.06	0.83	0.96	0.93	0.97	0.85	0.08	0.09	0.19	0.58	0.25
ECHAM3	0.31	0.64	0.62	0.40	0.86	0.84	0.48	0.37	0.51	0.83	0.14
ECHAM4	0.24	0.59	0.78	0.79	0.98	0.87	0.43	0.16	0.19	0.48	0.43
HadCM2	0.83	0.00	0.75	0.80	0.99	0.89	0.91	0.23	0.31	0.90	0.42
HadCM3	0.85	0.08	0.07	0.17	0.93	0.90	0.98	0.00	0.10	0.47	0.09
PCM	0.70	0.19	0.00	0.03	0.80	n/a	n/a	n/a	n/a	n/a	n/a

Pacific and a minimal increase or small decrease in far western Pacific, but without the Brazilian decrease and west-coast-USA increase. ECHAM4 shows a strong precipitation decrease over Brazil and a strong increase in the central Pacific, with a weaker increase over Indonesia, so it also has some elements of an El Niño-like response.

The first qEOF of the precipitation response represents that portion of the local precipitation variability that is correlated with changes in the global-mean precipitation. As seen from Table 10, $qEOF_1$ accounts for less of the space-time variability than EOF_1 for every model except HadCM2, where it accounts for 40% of the variability. Only a small part (1–6%) of total space-time variability in the aerosol effect is correlated with changes in global-mean precipitation, as indicated by the aerosol $qEOF_1$ values given in the last column of Table 10.

Table 11 is organized as follows: columns A and B compare control EOF_1 ($cEOF_1$) with CO_2 EOF 1 and 2; columns C-E intercompare three different measures of the effect of global warming on precipitation; columns F and G compare aerosol EOF_1 ($aEOF_1$) with control and CO_2 EOF_1; columns H-J intercompare three different measures of the effect of aerosols on the global precipitation field; and columns G and K represent two ways of comparing the effect of CO_2 and aerosols on precipitation. The salient results are as follows:

1. In four of the models (CCSR, HadCM2, HadCM3, PCM), $gEOF_1$ is highly correlated with $cEOF_1$ and in one model (CSIRO) there is almost zero correlation. In the latter case, $cEOF_1$ is highly correlated with $gEOF_2$. That is, a new mode of variation, associated with global warming and responsible for 14% of the space-time variation, arises in CSIRO, and the former primary mode of variability drops to second in importance but with little change in its structure.
2. In two models (CCC and CSIRO), the three measures of the change in precipitation in response to CO_2 are almost perfectly correlated with one another. However, none of these measures represents more than about 25–30% of the total space-time variation (and often much less). This is in contrast to temperature, where EOF_1 or $qEOF_1$ represent 64–93% of the space-time response to a CO_2 increase. The correlation between precipitation $qEOF_1$ and $\Delta P_{2070\text{-}99}$ is consistently higher ($R^2 \geq 0.8$) than between any other

pair of measures. HadCM2 is the only model where the three measures of the effect of aerosols on precipitation are highly correlated with each other *and* where $gEOF_1$ is highly correlated with $cEOF_1$.

3. Aerosol EOF_1 is consistently highly correlated with control EOF_1. That is, the year-by-year differences between the CO_2 and CO_2 + aerosol runs are dominated by the internal variability that is common to both runs and little changed from the control run, rather than by a persistent effect of aerosols on the pattern of precipitation. This does not mean that there is not a characteristic response pattern for aerosol forcing, but rather, that the low signal strength is masked by the amplification of noise that occurs when differences are taken. Aerosol EOF_1 resembles $gEOF_1$ only when the latter resembles $cEOF_1$. This is in contrast to temperature, where a response pattern distinctly different from the control run variability is evident in both $gEOF_1$ and $aEOF_1$. The correlation between aerosol $qEOF_1$ and $\Delta P_{2070\text{-}99}$ is consistently higher than between any other pair of measures, but not as high as for CO_2 $qEOF_1$ and $\Delta P_{2070\text{-}99}$. Finally, there is generally little correlation ($R^2 \leq 0.43$) between the 30-year average effect of aerosols and of CO_2 on precipitation at the end of the simulations.

Table 12 gives the common variance between CO_2 and CO_2 + aerosol runs for two measures of precipitation patterns: EOF_1 and $\Delta P_{2070\text{-}99}$. By either measure, the correlations between CO_2 and CO_2 + aerosol response patterns are quite high (R^2 = 0.78–0.96) for all models except ECHAM3 and ECHAM4. These models also have lower correlations than the other models for temperature. For all models, the CO_2/CO_2 + aerosols correlations are smaller than for temperature (see Table 3).

Finally, Table 13 gives the 2D pattern correlation between EOF_1 of the different models, and between $\Delta P_{2070\text{-}99}$ of the different models. There is remarkably little correlation among the models (R^2 = 0.00–0.46 for EOF_1, and R^2 = 0.00–0.28 for $\Delta P_{2070\text{-}99}$), in contrast to temperature (R^2 = 0.22–0.71 for EOF_1, Table 5).

Table 12 Common variance (R^2) between CO_2 (g) and CO_2 + aerosol (ga) $EOF_1$and precipitation change fields

	$gEOF_1$versus $gaEOF_1$	$g\Delta P_{2070–99}$ versus $ga\Delta P_{2070–99}$
CCC	0.93	0.87
CCSR	0.96	0.92
CSIRO	0.78	0.82
ECHAM3	0.23	0.14[a]
ECHAM4	0.42	0.61[b]
HadCM2	0.96	0.87
HadCM3	0.94	0.81

[a]Based on 2010–39 averages for both runs
[b]Based on 2040–69 averages for both runs

6.2 Absolute and percentage changes in precipitation

Because the leading EOF and qEOF account for so little of the space-time variation in the precipitation response to CO_2 forcing, we have examined in some detail the absolute and percentage change in total precipitation. Figure 20 compares the absolute zonal-mean precipitation for the control, CO_2, and CO_2 + aerosol runs for three representative models (CCC, CCSR, ECHAM3). All models show additional precipitation on the poleward side of the mid-latitude precipitation maxima in each hemisphere. These shoulders of additional precipitation may or may not be associated with a shift in the latitudes of maximum precipitation. The intertropical maximum in zonal-mean precipitation increases, but the absolute increase is never more than the absolute increase at high latitudes. This is because the major change in precipitation in the intertropical convergence zone is an east-west shift in precipitation, rather than an overall increase. In four models (CCSR, CSIRO, ECHAM4, HadCM2) there is pronounced increase in precipitation on the southern side of the intertropical maximum, as illustrated in Fig. 20 for CCSR, but any increases on the northern side are much smaller. The impact of aerosols is generally to uniformly reduce the change in zonal-mean precipitation caused by CO_2, except around 30°N, where aerosols either suppress any increase in precipitation caused by a CO_2 increase (e.g. CCC), or turn the increase into a decrease (as shown for ECHAM3). The largest net effect of aerosols on zonal-mean precipitation is that shown in Fig. 20 for ECHAM3 at 30°N. As noted earlier, aerosols in ECHAM3 have a particularly strong effect in suppressing the warming in a latitude band centered at 35°N.

Table 13 Common variance (R^2) between CO_2 precipitation EOF_1 and $\Delta P_{2070–99}$ of different models. Values above the diagonal are the correlations between the EOF_1 fields, while values below the main diagonal are the correlations between the $\Delta P_{2070–99}$ fields

	CCC	CCSR	CSIRO	ECHAM3	ECHAM4	HadCM2	HadCM3	PCM
CCC		0.14	0.03	0.00	0.00	0.25	0.05	0.00
CCSR	0.05		0.05	0.03	0.21	0.46	0.27	0.09
CSIRO	0.02	0.07		0.01	0.09	0.04	0.02	0.01
ECHAM3	0.00	0.05	0.12		0.01	0.07	0.09	0.00
ECHAM4	0.00	0.13	0.08	0.03		0.28	0.09	0.12
HadCM2	0.13	0.19	0.03	0.05	0.13		0.40	0.01
HadCM3	0.01	0.11	0.10	0.04	0.28	0.07		0.10
PCM	0.00	0.00	0.02	0.11	0.00	0.02	0.00	

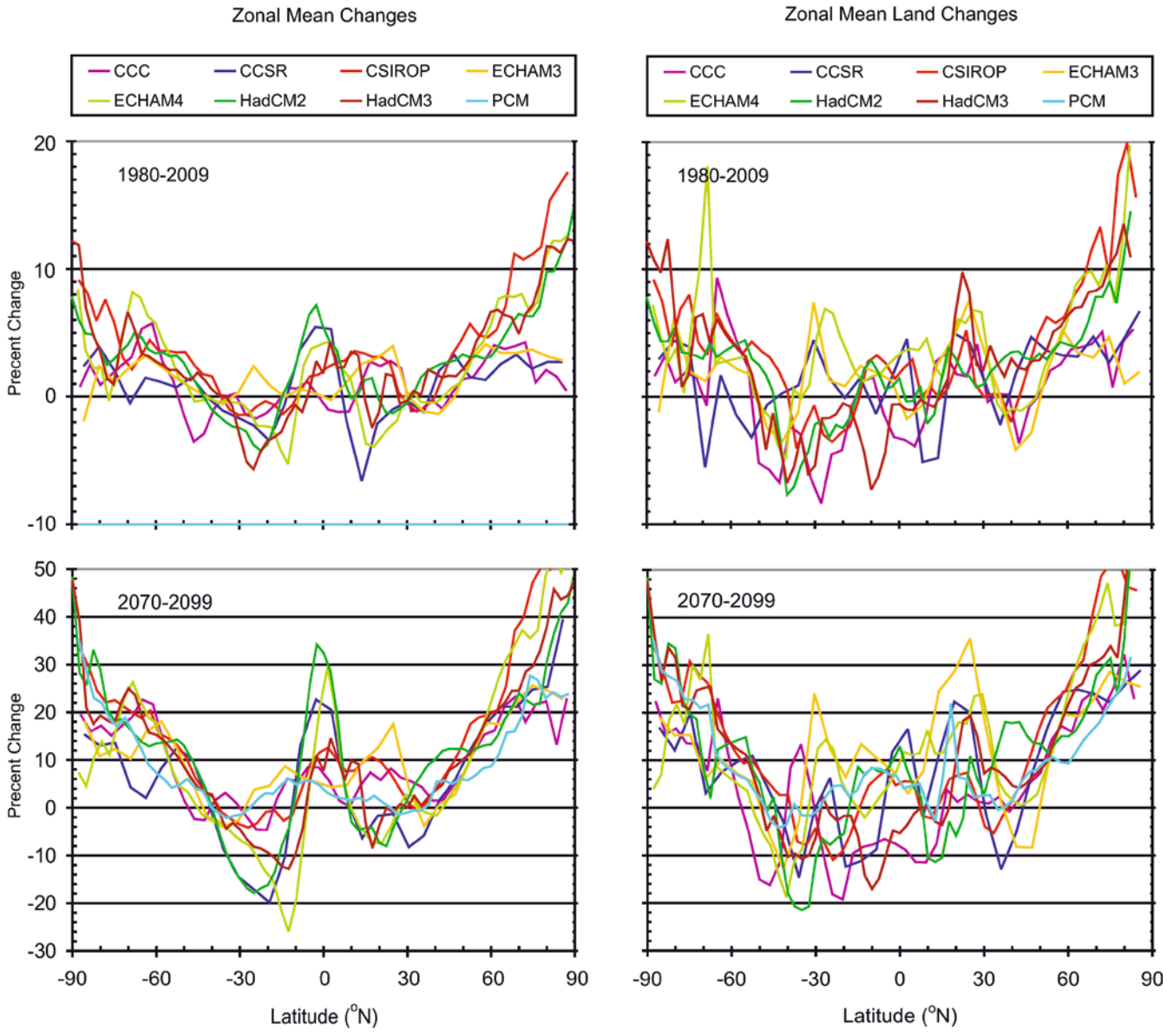

Fig. 21 Zonal-mean percentage change in precipitation (mm/day) for the CO_2 runs, relative to the 1890–1919 period, as simulated by the eight AOGCMs and averaged over the periods 1980–2009 and 2070–2099 (2070–79 for ECHAM3). For PCM, the changes are relative to the period 1960–1989 and are for the CO_2 + aerosol run. *Left*: ocean + land; *right*: land

Figure 21 gives the latitudinal variation in the percent change in zonal-mean precipitation, relative to the 1890–1919 period, for the periods 1980–2009 and 2070–99. In all of the models except ECHAM3, there are minima in the percent precipitation change somewhere in the regions 20–40°N and 20–40°S, with a maximum in the precipitation change between these two regions. The percent change in precipitation also increases more-or-less continuously as one moves poleward from these two regions, particularly for the 2070–99 period. There are particularly large percentage increases (25–30%) in zonal-mean precipitation in a narrow band in the tropics in CCSR, ECHAM4, and HadCM2, but as seen from Fig. 20 for CCSR, these are associated with an increase to the south of the tropical maximum in zonal-mean precipitation, rather than with an increase in the maximum zonal-mean precipitation. Decreases in NH subtropical precipitation of 5–10% occur in these models. There is considerably more scatter among the models in the latitudinal profile over land than for zonal-mean precipitation.

6.3 Scaling approximation to estimate regional decadal-mean changes in precipitation

The grid-point decadal-mean precipitation changes can be estimated by scaling the 2070–2099 precipitation-change pattern ($\Delta P_{2070–99}$) by the ratio of the change in global-mean decadal temperature to the change in glo-

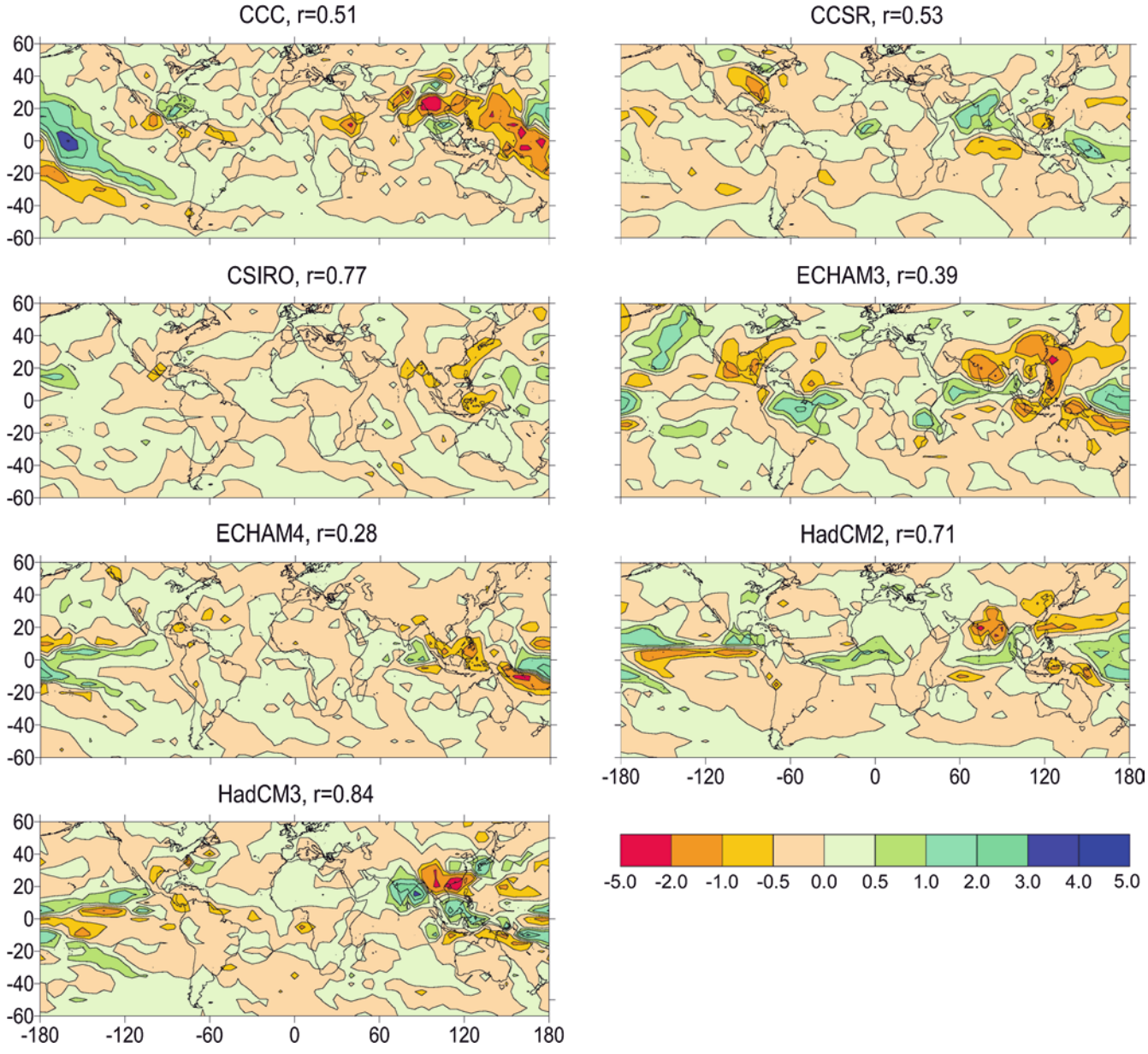

Fig. 22 Geographical variation in the excess aerosol effect on precipitation (mm/day), as defined in the main text, for the period 2070–2099 (2040–49 for ECHAM3 and ECHAM4)

bal-mean temperature over the period 2070–2099, or by scaling the dimensionless precipitation EOF_1 by the global mean 2070–2099 precipitation change times the foregoing ratio. The common variance between EOF_1 and $\Delta P_{2070–99}$ is very low in some models (Table 11, Column D), so these two fields represent separate estimators of the decadal precipitation change patterns (in contrast, $qEOF_1$ and $\Delta P_{2070–99}$ are much more similar). The global- mean RMSEs in the estimated decadal-mean precipitation were computed for each decade, and the average of these global-mean errors for all decades from 1900–10 to 2070–99 is given in Table 4 along with the RMS precipitation changes during the last decade of the simulation.

For models where precipitation EOF_1 and $\Delta P_{2070–99}$ are modestly ($R^2 \geq 0.4$) correlated (i.e. all models except HadCM3 and PCM), the errors are comparable when scaling EOF_1 or $\Delta P_{2070\text{-}99}$. However, in cases where there are substantial differences between EOF_1 and $\Delta P_{2070\text{-}99}$, use of $\Delta P_{2070–99}$ gives a substantially smaller error. This is in contrast to temperature, where scaling EOF_1 consistently gives smaller errors. The precipitation RMSEs are 25–35% of the RMS changes by the end of the simulation, in contrast to temperature, where the RMSEs are less than 5–10% of the RMS changes by the end of the simulation. However, the standard deviation of precipitation in the control run is also larger. In no more than 14–29% of the land grid points (depending on

the model) is the largest error for any decade greater than one standard deviation of the 10-year means in the control run, and in no more than 8–18% of the grid points is the largest decadal error greater than two standard deviations. These excess values are smaller than for temperature and are about what one would expect from chance. Thus, although scaling a fixed precipitation pattern is less successful in predicting the decadal-mean changes in precipitation than scaling a fixed temperature pattern to predict decadal-mean changes in temperature, the errors are statistically indistinguishable from zero.

Also given in Table 4 are the RMSEs when the CO_2 EOF_1 and $\Delta P_{2070–99}$ patterns are used to predict decadal-mean precipitation changes for the CO_2 + aerosol runs. In this case, the scaling of the CO_2 EOF_1 or $\Delta P_{2070–99}$ fields involves the ratio of the global-mean temperature change for the CO_2 + aerosol run during a given decade to the change in global-mean temperature over the period 2070–2099 for the CO_2 run. In most cases, the EOF_1 or $\Delta P_{2070–99}$ patterns from the CO_2 and CO_2 + aerosol runs are highly correlated with one another, so one would expect scaling of the CO_2 patterns to work as well in predicting CO_2 + aerosol precipitation changes as in predicting CO_2 precipitation changes (within statistical uncertainty). As seen from Table 4, the RMSEs tend to be smaller when predicting CO_2 + aerosol precipitation changes than when predicting CO_2 precipitation changes. The smaller errors in the former case can be largely explained by the smaller overall precipitation changes when aerosol forcing is included, and by the fact that the errors are large in both cases due to a significant noise component (this component of the error would be the same for CO_2 and CO_2 + aerosol runs, and would dilute any difference in the RMSEs).

6.4 Regional aerosol effects on precipitation

In spite of the similarity in the CO_2 and CO_2 + aerosol precipitation-change fields in the global mean, and in the RMSEs when using the CO_2 fields to predict CO_2 or CO_2 + aerosol precipitation changes, there could be discernable impacts of aerosols at the regional scale in the model results analyzed here. The Asian summer monsoon, for example, is dependent on the development of a temperature contrast between the Asian landmass and the adjacent ocean. The presence of aerosols over the Asian landmass could reduce the development of this temperature contrast, thereby weakening the Asian summer monsoon, as found by Meehl et al. (1996) in a predecessor to PCM, and by Mitchell and Jones (1997) in HadCM2. It should be noted, however, that change in land-sea temperature contrast is only one factor affecting the Asian monsoon. Changes in atmospheric water vapour content can over-ride the impact of changes in circulation, as shown by Douville et al. (2000) in an intercomparison of the effect of increasing CO_2 on the monsoon in four AGCMs driven by prescribed (and identical) changes in sea surface temperature. Of course, aerosols also affect the atmospheric water vapour content, but this is more of a global than a regional effect.

The detection of regional aerosol effects on precipitation is complicated by the fact that aerosols will tend to reduce changes in precipitation everywhere by virtue of the fact that the overall warming is lower in the presence of aerosols. Thus, if an impact of global warming is to increase precipitation in monsoon regions (as it does in the annual mean in some models, according to Fig. 18), the inclusion of aerosols will reduce monsoon precipitation compared to the case without aerosols. Thus, to detect a regional effect of aerosols, the precipitation change for the case with aerosols should be compared to the change that would be expected if the CO_2 pattern were scaled uniformly by the reduced global precipitation change in the presence of aerosols.

The regional "excess" effect of aerosols on temperature at point (x,y), $A_e(x,y)$, is computed here as

$$A_e(x,y) = \Delta P_{ga}(x,y) - \frac{\Delta\overline{P_{ga}}}{\Delta\overline{P_g}}\Delta P_g(x,y) \quad (1)$$

where $\Delta P_{ga}(x,y)$ and $\Delta P_g(x,y)$ are the local precipitation changes for CO_2 + aerosol and CO_2 runs, respectively, and $\Delta\bar{P}_{ga}$and $\Delta\bar{P}_{ga}$are the corresponding global-mean changes. Figure 22 gives $A_e(x,y)$ fields for the period 2070–2099 (or 2040–49 in the case of ECHAM3 and ECHAM4). Also given, at the top of each map, is the value of $\Delta P_{ga}/\Delta P_g$. This ratio ranges from 0.28 to 0.84 (i.e. the increase in global-mean precipitation in the presence of aerosols is as little as 28% of the increase that occurs due to CO_2 alone).

The global-mean value of $A_e(x,y)$ is zero by definition, so regions of rainfall deficit will be offset by regions of rainfall surplus. In four models (CCC, ECHAM3, HadCM2, and HadCM3) there is a rainfall deficit due to aerosols over at least part of the Asian monsoon region (see Fig. 22). In HadCM3, a rainfall deficit in China occurs adjacent to a rainfall surplus in India. In two models (CSIRO and ECHAM4) there is a weak rainfall deficit over southeast Asia, while in CCSR there is a weak rainfall surplus.

In three models (ECHAM4, HadCM2, HadCM3), an ITCZ/SPCZ structure is seen in the pattern of rainfall surpluses and deficits, and the pronounced SPCZ that is seen in the CCC control run (see Harvey 2003) is evident in the rainfall surplus pattern. These patterns can be explained as follows. The change in global-mean precipitation is small compared to the regional increases or decreases in precipitation caused by increasing CO_2. Because the change in global-mean precipitation is a small residual, a modest change of precipitation in any given rainbelt would substantially change the global mean, and with it, the uniform scaling factor ($\Delta\bar{P}_{ga}/\Delta\bar{P}_{ga}$). Deviations from the scaled $\Delta P_g(x,y)$ field would then reflect the underlying control precipitation pattern, rather than some physical effect of aerosols, and could

be of either sign (as in the equatorial Pacific in ECHAM4, HadCM2, and HadCM3). This makes it difficult to be confident that a real effect of aerosols has been detected in the Asian monsoon region in those models where $A_e(x,y)$ is only weakly negative in this region.

Note that the model results studied here contain only the direct effect of non-absorbing aerosols. A number of studies have examined the effects of absorbing (sooty) aerosols on monsoon precipitation and have found stronger evidence of an impact (Chung et al. 2002; Menon et al. 2002). Other studies have considered non-absorbing aerosols but have included the effects of aerosols on cloud properties and lifetime (the indirect aerosol radiative forcing), and have also found an effect on monsoon precipitation (Meehl et al. 1996; Rotstayn et al. 2000; Williams et al. 2001; Rotstayn and Lohmann 2002).

7 Summary and conclusions

This work has examined the patterns of temperature and precipitation change associated with an increasing CO_2 concentration and with the direct effects of non-absorbing (sulfate) aerosols, as simulated by eight coupled AOGCMs. Particular emphasis has been placed on characterizing the responses with fixed response patterns that account for as large a fraction of the space-time response as possible.

The main conclusions arising from this study with regard to the temperature response are as follows:

1. The temperature response to increasing CO_2 alone, or to a combination of increasing CO_2 and aerosols, can be well represented by the first EOF of temperature, which in turn is almost identical to the first quasi-EOF (qEOF) of temperature or to the temperature change pattern averaged over the last 30 years (usually 2070–2099) of the simulations. EOF_1 accounts for 82–93% of the space-time response to increasing CO_2 in all models, and 65–90% of the response to a combination of increasing CO_2 and aerosols in six of the eight models.
2. The temperature response pattern to increasing CO_2 is highly correlated ($R^2 \geq 0.85$) with the temperature response pattern to a combination of CO_2 and aerosols in all models except ECHAM3 (but in this model, CO_2 + aerosol EOF_1 accounts for only 45% of the total space-time variance).
3. As a result of the above, the space-time variation in decadal-mean temperature to either CO_2 alone, or to CO_2 + aerosol, can be predicted by multiplying the response pattern obtained from the CO_2-only run (normalized to a global-mean warming of 1 K) times the global-mean warming of the CO_2 or CO_2 + aerosol run, validating the simple scaling method first suggested by Santer et al. (1990). RMSEs are 5–10% of the RMS temperature change by the end of the twentyfirst century.
4. There is a high degree of similarity in the response patterns of the models to increasing CO_2 (R^2 between EOF_1 of different models generally > 0.5), the common features being maximal warming at high NH latitudes, minimum warming around 60°S, greater warming over land than over ocean, and often greater warming in the eastern and/or central equatorial Pacific Ocean than in the western equatorial Pacific Ocean.
5. The impact of aerosols on temperature can be computed from EOF_1 of the year-to-year differences in temperature for the CO_2 and CO_2 + aerosol runs, from $qEOF_1$ of these differences, or from the difference in average temperature over the last 30 years of the CO_2 and CO_2 + aerosol runs (generally 2070–2099, with the difference designated as $\Delta T_{2070\text{-}99}$). In some cases (CCC, CSIRO, ECHAM3, HadCM2), these three measures are highly correlated with one another and with the temperature response pattern to increasing CO_2 alone.
6. In other cases (CCSR, ECHAM4, HadCM3), aerosol EOF_1 is poorly correlated with CO_2 EOF_1, but is modestly to highly correlated with control EOF_1 and poorly correlated with the other measures of the aerosol effect. That is, the year-to-year differences between the CO_2 and CO_2 + aerosol runs are dominated by internal variability rather than by the long-term temperature response pattern to aerosols. In these cases, aerosol EOF_2 tends to be modestly to highly correlated with CO_2 EOF_1.
7. In every case where EOF_1 and $qEOF_1$ differ from one another, $qEOF_1$ is better correlated with $\Delta T_{2070\text{-}99}$ than is EOF_1. This is re-assuring, given that $qEOF_1$ and $\Delta T_{2070\text{-}99}$ are the most physically direct measures of the effect of aerosols on temperature.
8. In every model except ECHAM3, the temperature response to aerosols, as represented by $qEOF_1$ or $\Delta T_{2070\text{-}99}$, is highly correlated with the temperature response to CO_2 alone. This implies that it will not be possible to separately detect the effects of increasing CO_2 and aerosols in the observed temperature record, using response patterns obtained from current AOGCMs, and that the detection results obtained with ECHAM3 (Hegerl et al. 2000) may not be valid.

The similarity between the temperature response to CO_2 and to aerosols arises because the local response is largely governed by regional feedback processes driven by the change in global-mean temperature, rather than by the pattern of radiative forcing (which differs markedly for CO_2 and aerosols). However, the similarity is also due to the fact that all of the models show greater warming in the Northern Hemisphere than in the Southern Hemisphere in response to increasing CO_2, and over land than over ocean. Since the aerosol radiative forcing (a cooling tendency) is also greater in the NH and over land, the aerosol response,even if dominated by the forcing pattern, will tend to be similar (but opposite in sign) to the response to CO_2.

The hemispheric asymmetry in the current generation of AOGCMs stands in contrast to the observed temperature trends over the period 1900–2002, which are nearly symmetric (Harvey and Wigley 2003). There are many possible reasons for this difference, which requires further investigation. In AOCGMs with a more hemispherically symmetric response to CO_2 or a suite of GHGs, it may be that there will be greater difference in the temperature response patterns to increasing GHGs and to aerosols. This is critical to the ability to detect separate aerosol and GHG effects on climate, and to be able to constrain the magnitude of present aerosol radiative forcing. The recent analysis by Harvey and Kaufmann (2002), for example, assumes (based on simulations with an energy balance climate model coupled to a 2D ocean model) that there is a difference in the effect of increasing GHGs and industrial aerosols on the difference between NH and SH temperature.

The main conclusions arising from this study with regard to the precipitation response are as follows:

1. The precipitation response to increasing CO_2 is substantially noisier than the temperature response. As a result, precipitation EOF_1 accounts for only 10–30% of the space-time variance in the CO_2 runs.
2. CO_2 EOF_1 is generally highly correlated (R^2 as high as 0.85) with control EOF_1, which in turn represents El Niño-like precipitation variability. In most models, there is a long-term increase in amplitude of EOF_1 in the CO_2 run, indicating a more El Niño-like precipitation pattern as the climate warms. This includes substantial decreases over the Brazilian Amazon in four of the eight models, with possibly important implications for the carbon cycle (see, e.g. Cox et al. 2000). This is consistent with the El Niño-like temperature response seen in the equatorial Pacific Ocean in most models.
3. In response to increasing CO_2, all of the models show an increase in zonal-mean precipitation in the Intertropical Convergence Zone and poleward of the mid-latitude precipitation maxima, and a decrease in bands at or near 30°S and 30°N (including the entire Mediterranean region and much or all of the Middle East in all models). Many models also show an eastward shift of the precipitation maximum in the western equatorial Pacific. There is substantial disagreement among the models in the placement of the maxima and minima, in the global-mean sensitivity of precipitation to increasing temperature (a factor of 3 variation), and in the relative precipitation increases over land and over ocean (in CCC, precipitation on average decreases over land until near the end of the simulation, but increases by 8% over oceans, while in ECHAM4, precipitation is largely unchanged over oceans but increases by 11% on average over land by 2100).
4. Aerosols have a disproportionally large effect in suppressing the increase in precipitation, compared to their effect in suppressing warming. There is evidence in some models that the non-absorbing aerosols considered here decrease summer monsoon compared to the changes that would be expected based on the globally-averaged effect of aerosols on precipitation.
5. When regional precipitation changes over time are predicted by scaling a fixed precipitation-change pattern with the global mean temperature change, the global mean RMSE in the predicted change in decadal-mean precipitation is 25–35% of the global RMS precipitation changes. Thus, there is some skill in using the pattern-scaling approach for precipitation. Comparable errors are obtained when the CO_2 pattern is used to predict precipitation changes for CO_2 or CO_2 + aerosol runs.

The results obtained here have important implications for the regional impacts of concurrent reductions in CO_2 and aerosol emissions. Although sooty aerosols have a warming effect on climate, the net effect of an increase in anthropogenic aerosols is likely to be one of cooling. A reduction in aerosol emissions will therefore tend to accelerate global warming during the first few decades following the reduction in emissions, due to the short lifespan (days) of aerosols in the atmosphere (as first suggested by Wigley 1991). However, based on the aerosol response patterns obtained in all of the models studied here except ECHAM3, the relative acceleration in warming will not be significantly larger than the global-mean acceleration in regions with high aerosol concentrations. This is because, in all models except ECHAM3, the temperature response pattern to aerosols is strongly correlated with the response pattern to CO_2. In ECHAM3, the acceleration in the warming will be disproportionately large in polluted regions because the calculated aerosol cooling for present conditions is concentrated in these regions in this model.

The impacts of global warming on natural ecosystems and on agriculture depend on both changes in temperature and changes in precipitation. Although a reduction in aerosol emissions will temporally accelerate global warming, it will also allow for a larger increase in rainfall, thereby partly mitigating the adverse short-term effect on temperatures. This mitigating factor is enhanced by the fact that, in all models, aerosols have a disproportionally larger effect in suppressing the increase in precipitation than in suppressing the increase in temperature. Their removal will therefore produce a larger rebound in precipitation than in temperature.

Acknowledgements This work benefited from many helpful comments by Tom Wigley. This research was supported by NSERC grant OGP0001413.

References

Andronova NG, Schlesinger ME (2000) Causes of global temperature changes during the nineteenth and twentieth centuries. Geophy Res Let 27: 2137–2140

Boer GJ, Flato G, Reader MC, Ramsden D (2000a) A transient climate change simulation with greenhouse gas and aerosol

forcing: experimental design and comparison with the instrumental record for the twentieth century. Clim Dyn 16: 405–425
Boer GJ, Flato G, Ramsden D (2000b) A transient climate change simulation with greenhouse gas and aerosol forcing: projected climate to the twenty-first century. Clim Dyn 16: 427–450
Chase TN, Pielke RA, Kittel TGF, Nemani RR, Running SW (2000) Simulated impacts of historical land cover changes on global climate in northern winter. Clim Dyn 16: 93–105
Chung CE, Ramanathan V, Kiehl JT (2002) Effects of the South Asian absorbing haze on the Northeast Monsoon and surface-air heat exchange. J Clim 15: 2462–2476
Cox PM, Betts RA, Jones CD, Spall SA, Toterdell IA (2000) Acceleration of global warming due to carbon-cycle feedbacks in a coupled climate model. Nature 408: 184–187
Douville H, Royer JF, Polcher J, Cox P, Gedney N, Stephenson DB, Valdes PJ (2000) Impact of CO_2 doubling on the Asian summer monsoon: Robust versus model-dependent responses. J Meteorol Soc Japan 78: 421–439
Emori S, Nozawa T, Abe-Ouchi A, Numaguti A, Kimoto M, Nakajima T (1999) Coupled ocean-atmosphere model experiments of future climate change with an explicit representation of sulfate aerosol scattering. J Meteorol Soc Japan 77: 1299–1307
Flato GM, Boer GJ (2001) Warming asymmetry in climate change simulations. Geophys Res Lett 28: 195–198
Harvey LDD (2000) Global warming: The hard science. Prentice Hall, Harlow, pp 336
Harvey LDD, Kaufmann RK (2002) Simultaneously constraining climate sensitivity and aerosol radiative forcing. J Clim 15: 2837–2861
Harvey LDD, Wigley TML (2003) Characterizing and comparing the control Run variability of eight coupled AOGCMs and of observations. Part 1: temperature. Clim Dyn 21: 619–646
Hegerl GC, Stott P, Allen M, Mitchell JFB, Tett SFB, Cubasch U (2000) Detection and attribution of climate change: sensitivity of results to climate model differences. Clim Dyn 16: 737–754
Hirst AC, Gordon HB, O'Farrell SP (1996) Global warming in a coupled climate model including oceanic eddy-induced advection. Geophys Res Lett 23: 3361–3364
Houghton JT, Din Y, Griggs DJ, Noguer M, van der Linden PJ, Dai X, Maskell K, Johnson CA (eds) (2001) Appendix II, SRES Tables. Climate change 2001: the scientific basis. Cambridge University Press, Cambridge UK, pp 800–826
Hulme M, Brown O (1998) Portraying climate scenario uncertainties in relation to "tolerable" regional climate change. Clim Res 10: 1–14
Hulme M, Raper SCB, Wigley TML (1995) An integrated framework to address climate change (ESCAPE) and further developments of the global and regional climate modules (MAGICC). Energy Policy 23: 347–355
Huntingford C, Cox PM (2000) An analogue model to derive additional climate change scenarios from existing GCM simulations. Clim Dyn 16: 575–586
Johns TC, Carnell RE, Crossley JF, Gregory JM, Mitchell JFB, Senior CA, Tett SFB, Wood RA (1997) The second Hadley Centre coupled ocean-atmosphere GCM: model description, spinup and validation. Clim Dyn 13: 103–134
Kelly PM, Jones PD, Pengqun J (1999) Spatial patterns of variability in the global surface air temperature data set. J Geophys Res 104: 24,237–23,256
Leggett J, Pepper WJ, Swart RJ, Edmonds JA, Meira Filho LG, Mintzer I, Wang MX, Wasson J (1992) Emissions scenarios for the IPCC: an update. In: Houghton JT, Callander BA, Varney SK (eds), Climate change 1992: the supplementary report to the IPCC scientific assessment. Cambridge University Press, Cambridge UK, pp 69–95
Meehl GA, Washington WM, Erickson DJ, Briegleb BP, Jaumann PJ (1996) Climate change from increased CO_2 and direct and indirect effects of sulfate aerosols. Geophys Res Lett 23: 3755–3758
Menon S, Hansen J, Nazarenko L, Luo Y (2002) Climate effects of black carbon aerosols in China and India. Science 297: 2250–2253
Mitchell JFB, Johns TC (1997) On modification of global warming by sulfate aerosols. J Clim 10: 245–267
Mitchell JFB, Johns TC, Eagles M, Ingram WJ, Davis RA (1999) Towards the construction of climate change scenarios. Clim Change 41: 547–581
Mitchell TD (2003) Pattern scaling: an examination of the accuracy of the technique for describing future climate. Clim Change 60: 217–242
Nakićenović N et al. (2000) IPCC special report on emissions scenarios. Cambridge University Press, Cambridge UK, pp 599
Pitman AJ, Zhao M (2000) The relative impact of observed change in land cover and carbon dioxide as simulated by a climate model. Geophys Res Lett 27: 1267–1270
Qian Y, Giorgi F (1999) Interactive coupling of regional climate and sulfate aerosol models over eastern Asia. J Geophys Res 104 (D6): 6477–6499
Räisänen J (1997) Climate response to increasing CO_2 and anthropogenic sulphate aerosols–comparison between two models. Department of Meteorology, University of Helsinki Rep 46, pp 80
Reader MC, Boer GJ (1998) The modification of greenhouse gas warming by the direct effect of sulphate aerosols. Clim Dyn 14: 593–607
Roeckner E, Bengtsson L, Feichter J, Lelieveld J, Rodhe H (1999) Transient climate change simulations with a coupled atmosphere-ocean GCM including the tropospheric sulfur cycle. J Clim 12: 3004–3032
Rotstayn LD, Lohmann U (2002) Tropical rainfall trends and the indirect aerosol effect. J Clim 15: 2103–2116
Rotstayn LD, Ryan BF, Penner JE (2000) Precipitation changes in a GCM resulting from the indirect effects of anthropogenic aerosols. Geophys Res Lett 27: 3045–3048
Santer BD, Wigley TML, Schlesinger ME, Mitchell JFB (1990) Developing climate scenarios from equilibrium GCM results. Rep 47, Max-Planck Institut für Meteorolgie, Hamburg, Germany, pp 29
Santer BD, Wigley TML, Meehl GA, Wehner MF, Mears C, Schabel M, Wetnz FJ, Amman C, Arblaster J, Bettge T, Washington WM, Taylor KE, Boyle JS, Bruggemann W, Doutriaux C (2003a) Influence of satellite data uncertainties on the detection of externally-forced climate change. Science 300: 1280–1284
Schlesinger ME, Malyshev S, Rozanov EV, Yang F, Andronova NG, de Vries B, Grübler A, Jiang K, Masui T, Morita T, Penner J, Pepper W, Sankovski A, Zhang Y (2000) Geographical distributions of temperature change for scenarios of greenhouse gas and sulfur dioxide emissions. Technol Forecast Soc Change 65: 167–193
Tett SFB, Stott PA, Allen MA, Ingram WJ, Mitchell JFB (1999) Causes of twentieth century temperature change. Nature 399: 569–572
Timmermann A, Latif M, Grötzner A, Voss R (1999) Modes of climate variability as simulated by a coupled general circulation model. Part I: ENSO-like climate variability and its low-frequency modulation. Clim Dyn 15:605–618
Wigley TML (1991) Could reducing fossil-fuel emissions cause global warming? Nature 349: 503–506
Williams KD, Jones A, Roberts DL, Senior CA, Woodage MJ (2001) The response of the climate system to the indirect effects of anthropogenic sulfate aerosols. Clim Dyn 17: 845–856
Yu B, Boer GJ (2002) The roles of radiation and dynamical processes in the El Niño-like response to global warming. Clim Dyn 19: 539–553